Article

Effect of High Energy Ball Milling Time on the Density and Mechanical Properties of W-7%Ni-3%Fe Alloy

A. V. Nokhrin *, N. V. Malekhonova *, V. N. Chuvil'deev, N. V. Melekhin, A. M. Bragov, A. R. Filippov, M. S. Boldin, E. A. Lantsev, N. V. Sakharov

Materials Science Department, Physical and Technical Research Institute, Lobachevsky State University of Nizhny Novgorod, 603022, Nizhny Novgorod, Russia; nokhrin@nifti.unn.ru (A.V.N.); malekhonova@nifti.unn.ru (N.V.M.1); chuvildeev@nifti.unn.ru (V.N.C.); melehin@nifti.unn.ru (N.V.M.2); bragov@mech.unn.ru (A.M.B.); filippov@mech.unn.ru (A.R.F.); boldin@nifti.unn.ru (M.S.B.); elancev@nifti.unn.ru (E.A.L.); nvsaharov@nifti.unn.ru (N.V.S.)

* Correspondence: nokhrin@nifti.unn.ru (A.V.N.); malekhonova@nifti.unn.ru (N.V.M.1).

Abstract: The present work was aimed at the investigation of effect of High Energy Ball Milling (HEBM) time on the sintering kinetics, structure, and properties of heavy tungsten alloy (HTA) W-7%Ni-3%Fe. The HTA samples were obtained from the nanopowders (20-80 nm) by conventional liquid phase sintering (LPS) in hydrogen and by Spark Plasma Sintering (SPS) in vacuum. The HTA density was shown to depend on the HEBM time non-monotonously that originates from the formation of non-equilibrium solid solutions in the W-Ni-Fe systems during HEBM. The SPS kinetics of the HTA nanopowders was shown to have a two-stage character, the intensity of which depends on the Coble diffusion creep rate and on the intensity of diffusion of the tungsten atoms in the crystal lattice of the γ-phase. The kinetics of sintering of the initial submicron powders have a single-stage character originating from the intensity of the grain boundary diffusion in the γ-phase. The dependencies of the hardness and of the yield strength on the grain sizes were found to obey the Hall-Petch relation. The hardness, strength, and dynamic strength in the compression tests of the fine-grained tungsten alloys obtained by SPS and LPS were studied.

Keywords: tungsten alloys; nanopowders; high energy ball milling; spark plasma sintering; strength

1. Introduction

Heavy tungsten alloys (HTAs) of the W-Ni-Fe system with the W contents over 85-90% have a number of unique characteristics: simultaneous increased density, strength, and plasticity at room temperature [1-5], high characteristics of dynamic strength [6, 7], high radiation resistance, etc. The industrial tungsten alloys with 90-95%W obtained by conventional liquid-phase sintering (LPS) have the density of 17-19 g/cm^3, the ultimate strength up to 1000 MPa, and elongation to failure up to 25-30% at room temperature. Additional strain strengthening allows improving the ultimate strength up to 1400-1600 MPa preserving satisfactory ductility [8-11]. These features make HTAs interesting for various construction applications as well as interesting object for investigations of the effect of the interphase boundaries on the mechanical properties of the alloys [12-15].

It is worth noting that the technologies of strain hardening of the HTAs have approached the limits of their capabilities at present. For further improving the properties of the HTA, modern technologies of powder metallurgy are used often [16, 17] including the additive manufacturing methods [18-20] and microwave sintering method [21]. Modern methods of fabrication of nanopowder compositions W-Ni-Fe are being developed extensively [5,18,22].

The analysis of the literature shows Spark Plasma Sintering (SPS) to be one of promising methods of fabricating the HTAs [23-27]. An opportunity to vary main process parameters affecting the microstructure parameters of the HTAs most essentially (the heating rate, the temperature and time of sintering, the magnitude of the pressure applied, etc.) directly in the course of sintering provides a great flexibility to SPS method in controlling the mechanical properties of the HTAs. An opportunity of sintering the materials at very high heating rates (up to 2500 °C/min) is an important

Preprints (www.preprints.org) | NOT PEER-REVIEWED | Posted: 18 April 2023 doi:10.20944/preprints202304.0503.v1

feature of SPS technology, which allows reducing the grain growth rate [23,27]. The fine-grained HTAs obtained by SPS have simultaneously high strength and hardness [28-44] (Table A1, see Appendix A).

Joint application of High Energy Ball Milling (HEBM) and SPS is one of promising methods of further improving the mechanical properties of the HTAs [1,2,8,9,12-17]. This allows ensuring an outstanding increase in the strength and hardness of the HTAs (Table A1, see Appendix A). It is interesting to note that the results of [27,28,33,39] evidence the possibility of formation of strongly supersaturated solid solution of tungsten in the γ-phase based on nickel during HEBM that leads to an additional acceleration of sintering of the W-based nanopowders. The formation of the supersaturated solid solution of tungsten atoms in the γ-phase leads to manifestation of some unexpected effects. The effect of non-monotonous dependence of the density on the sintering temperature [28, 29, 35,43-45] as well as the effect of reduction of the activation energy of sintering of the nanopowders [45] deserve high attention. One should note separately the effect of decreasing of the density of the tungsten alloys sintered from mechanically activated nanopowders [33,39,45], the nature of which remains unclear now. Also, the effect of nonmonotonous (with a maximum) dependencies of the HTA density on the time of preliminary HEBM of the powders observed in [45] is interesting.

From the practical viewpoint, the result of increase in the hardness, the static strength and the dynamic one of the HTAs obtained by SPS is important.

The analysis of the literature shows that the W-7%Ni-3%Fe alloys obtained by SPS from nanopowders (t_{HEBM} = 20 min) have a higher dynamic strength as compared to the coarse-grained alloys [42, 46]. The decreasing of the grain sizes was noted to result in simultaneous increase in the static strength, the dynamic one, and in the penetration depth of a HTA sample into a steel barrier. At the throwing speed of 1194 m/s, the penetration depth reached 15.2 mm whereas for the coarse-grained HTAs this magnitude varied from 9.4 to 12.8 mm at similar testing regimes [46]. The formation of strongly supersaturated solid solution in the γ-phase may be one of the origins of manifestation of increased dynamic strength of the HTAs. In our opinion, it allows increasing the strength of the interphase (α-γ)-boundaries and, as a consequence, ensuring additional increase in the strength of HTAs.

The investigation of the effect of the HEBM time (t_{HEBM}) of the powders on the density, microstructure parameters, and mechanical properties of heavy tungsten alloy W-7%Ni-3%Fe obtained by SPS was the main goal of the present work.

2. Materials and Methods

The object of investigations was W-7%Ni-3%Fe alloy. The chemical compositions of the initial powders α-W, β-Ni, and α-Fe are presented in Table 1. The mean particle sizes in the initial powders α-W, β-Ni, and α-Fe according to Fischer were R_0 = 0.8 μm, 20 μm, and 11 μm respectively.

Table 1. Chemical composition of initial powders (wt.%).

Powders	O	Fe	C	S	P	Ni	Co	Si	Cu	Mo	Mn
α-W	$8\cdot10^{-2}$	$2\cdot10^{-2}$	$1\cdot10^{-2}$	-	$5\cdot10^{-3}$	$1\cdot10^{-2}$	-	$5\cdot10^{-3}$	$1\cdot10^{-2}$	$4.5\cdot10^{-2}$	$2\cdot10^{-3}$
β-Ni	$3\cdot10^{-1}$	$1.5\cdot10^{-3}$	$1\cdot10^{-1}$	$6\cdot10^{-4}$	$1\cdot10^{-3}$	-	$7\cdot10^{-4}$	$1\cdot10^{-3}$	$1\cdot10^{-3}$	-	$3\cdot10^{-4}$
α-Fe	$2\cdot10^{-1}$	-	$4.8\cdot10^{-2}$	$4\cdot10^{-3}$	-	-	-	$1\cdot10^{-2}$	-	-	-

The initial coarse-grained compositions were obtained by mixing the powders α-W, β-Ni, and α-Fe in a FRITSCH® Pulverisette 6 planetary ball mill (Idar-Oberstein, Germany). The mixing time was 15 h, the mixing rate was 100 rpm. HEBM of the compositions W-7%Ni-3%Fe was performed in APF-3 high energy planetary mill (Russia). The acceleration of the milling bodies was 60g, the mixing rate was 1450 rpm. The containers and milling balls of 6-10 mm in diameter were made from industrial alloy W-7%Ni-3%Fe. The mass ratio of the balls and the powders was 10:1. HEBM with the durations of 5, 10, 20, and 40 min was performed in argon ambient with addition of ethanol. To minimize the heating of the powders, HEBM was performed in several stages each 5 min long.

Preprints (www.preprints.org) | NOT PEER-REVIEWED | Posted: 18 April 2023 doi:10.20944/preprints202304.0503.v1

The HTA samples were obtained by conventional sintering in hydrogen (Method I) and by SPS (Method II).

To obtain the HTA samples by Method I, the nanopowders were pressed into the samples of 30 mm in diameter and 5-6 in height in advance. The uniaxial pressing by the pressure of 150 MPa was performed at room temperature in a steel mold. The sintering was performed in a two-stage regime: Stage I – heating with the rate 25 °C/min up to 950 °C and holding for 2 h for the reduction of the powders and removing oxygen; Stage II – heating up to the sintering temperature (1250, 1300, 1350, and 1400 °C) in 100 min and holding for t_s = 1 h. The accuracy of measuring the temperature was ±6 °C. After sintering, the samples were subjected to annealing in vacuum (10^{-5} Torr) at 1000 °C, 2 h. As the reference samples, the coarse-grained alloys W-7%Ni-3%Fe obtained by sintering the coarse-grained powder compositions in hydrogen were used.

Method II was implemented using Dr. Sinter model SPS-625 setup (SPS SYNTEX Inc., Japan). The sintering of the samples of 30 mm in diameter and 4-4.5 mm in height was performed in vacuum (6 Pa) when applying a uniaxial pressure of 70 MPa. A single-stage sintering regime was used – heating with the rate of 100 °C/min up to the sintering temperature (1200 °C). The uniaxial pressure was applied simultaneously with the beginning of heating up. The holding at the sintering temperature was absent (t_s = 0 min). The temperature was measured by an optical pyrometer Chino IR-AH (Japan) focused onto the surface of the graphite mold. The uncertainty of the temperature measurement was ±5 °C. As the reference samples, the nanopowders after HEBM subjected to annealing in hydrogen at 900 °C, 1 h in advance (before SPS) were used.

In the course of heating up, the effective shrinkage (L_{eff}, mm) and shrinkage rate (S_{eff}, mm/s) of the nanopowders were measured using a dilatometer. The contribution of the thermal expansion (L_0, mm) of the graphite mold and punch was taken into account on the base of the results of experiments with empty mold. The temperature curves of shrinkage of the nanopowders (L, mm) were calculated according to the formula: $L(T) = L_{eff}(T) - L_0(T)$.

The residual graphite was removed from the surfaces of the sintered samples of 30 mm in diameter by waterjet cleaning. The mechanical grinding was performed using Struers Secotom 10 setup, polishing – Buehler Automet 250 setup. In the course of mechanical treatment, the layers of ~300-350 μm, were removed from the sample surfaces, which an increased carbon concentration can be observed in due to high temperature interaction of the material with the graphite mold [47,48].

The microstructure investigations of the alloys were carried out using Leica IM DRM optical metallographic microscope, Jeol JSM-6490 scanning electron microscope (SEM), and TESCAN Vega 2 SEM with Oxford Instruments INCA 350 EDS microanalyzer. The density of the samples was measured by hydrostatic weighting in distilled water using Sartorius CPA balance. The uncertainty of measuring the density was ± 0.01 g/cm^3. The magnitude of the theoretical density was accepted to be equal to ρ_{th} = 17.245 g/cm^3. The analysis of the chemical composition was performed using Ultima 2 ICP atomic-emission spectrometer and Leco RHEN-602 analyzer. The X-ray diffraction (XRD) phase analysis was performed using Shimadzu XRD-700 diffractometer (CuK_α emission, λ = 1.54056 Å, scan rate 0.5 °/min, exposure 2 s). The phase analysis of the samples was performed by Rietveld method. The contribution of the apparatus broadening into the XRD peaks was taken into account according to [45]. The analysis of internal stresses and calculation of the sizes of coherent scattering regions were performed by Williamson-Hall method [49].

To study the mechanical properties of the sintered samples, the stress-relaxation testing technique was used allowing determining the magnitudes of the macroelasticity stress (lattice friction stress) (σ_0) and of the yield strength (σ_y) in the compression tests [45]. To measure σ_0 and σ_y, the cylindrical samples of 3 mm in diameter and 6 in height were used. The uncertainties of measuring σ_0 and σ_y were ±20 MPa. The microhardness (Hv) of the alloys was measured using HVS-1000 hardness tester at the load of 1 kg.

The magnitude of compressive dynamic ultimate strength (Ys) was investigated by Kolsky bar method using Hopkinson split rod at the strain rate of ~10^3 s^{-1} [50]. An example of a dynamic strain curve of a tungsten alloy is presented in Fig. 1. The ballistic characteristics of the material were determined by measuring the penetration depth (H) of the sample of 3 mm in diameter and 25 mm

Preprints (www.preprints.org) | NOT PEER-REVIEWED | Posted: 18 April 2023 doi:10.20944/preprints202304.0503.v1

long (Fig. 2a) into a steel target of 30 in thickness. The penetration depth of the sample was measured on the metallographic cross-section with Leica IM DRM optical microscope using Good Grains software (Fig. 2b). The uncertainty of determining the magnitude of H was ± 0.01 mm. The steel hardness was 27-30 HRC. The samples were accelerated with a 12 mm two-stage gas gun powered by compressed air. The impact angle of the sample with the steel plate was 90°. The test procedure was described in [46]. The samples for testing were cut out from the central parts of the workpieces of 30 mm in diameter by spark cutting in distilled water.

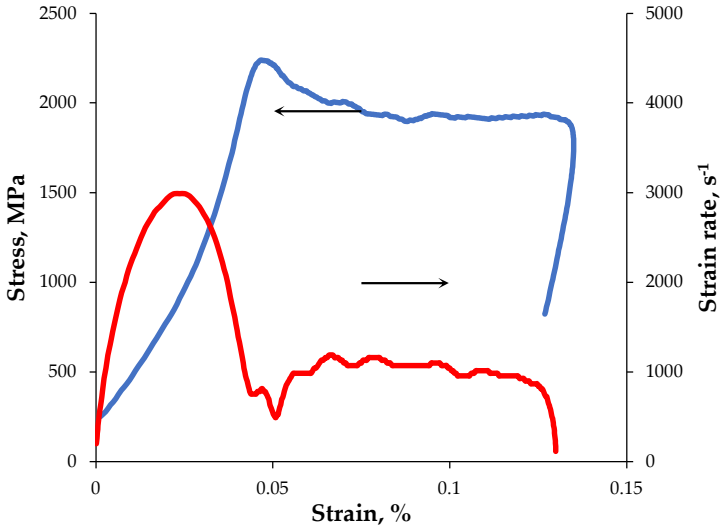

Figure 1. Typical stress – strain and strain rate – strain curves for a tungsten alloy sample recorded in a dynamic compression test according to Kolsky bar method.

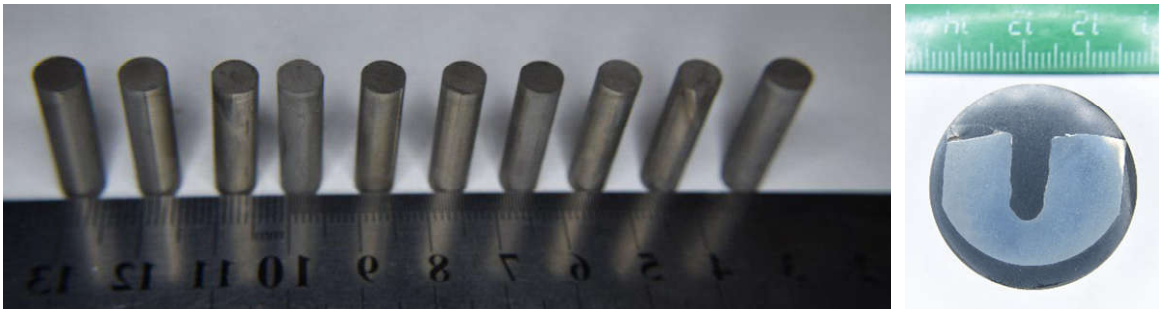

(a) **(b)**

Figure 2. Tungsten alloy samples for testing (**a**) and example of measuring the sample penetration depth into the steel target (**b**).

Preprints (www.preprints.org) | NOT PEER-REVIEWED | Posted: 18 April 2023 doi:10.20944/preprints202304.0503.v1

3. Results

3.1. Investigation of the powders`

Fig. 3 presents the images of the powders of W-7%Ni-3%Fe compositions in the initial state, after mixing in the FRITSCH® Pulverisette 6 planetary ball mill (32 h, Fig. 3a) and after HEBM for different processing times (Figs. 3b-3f).

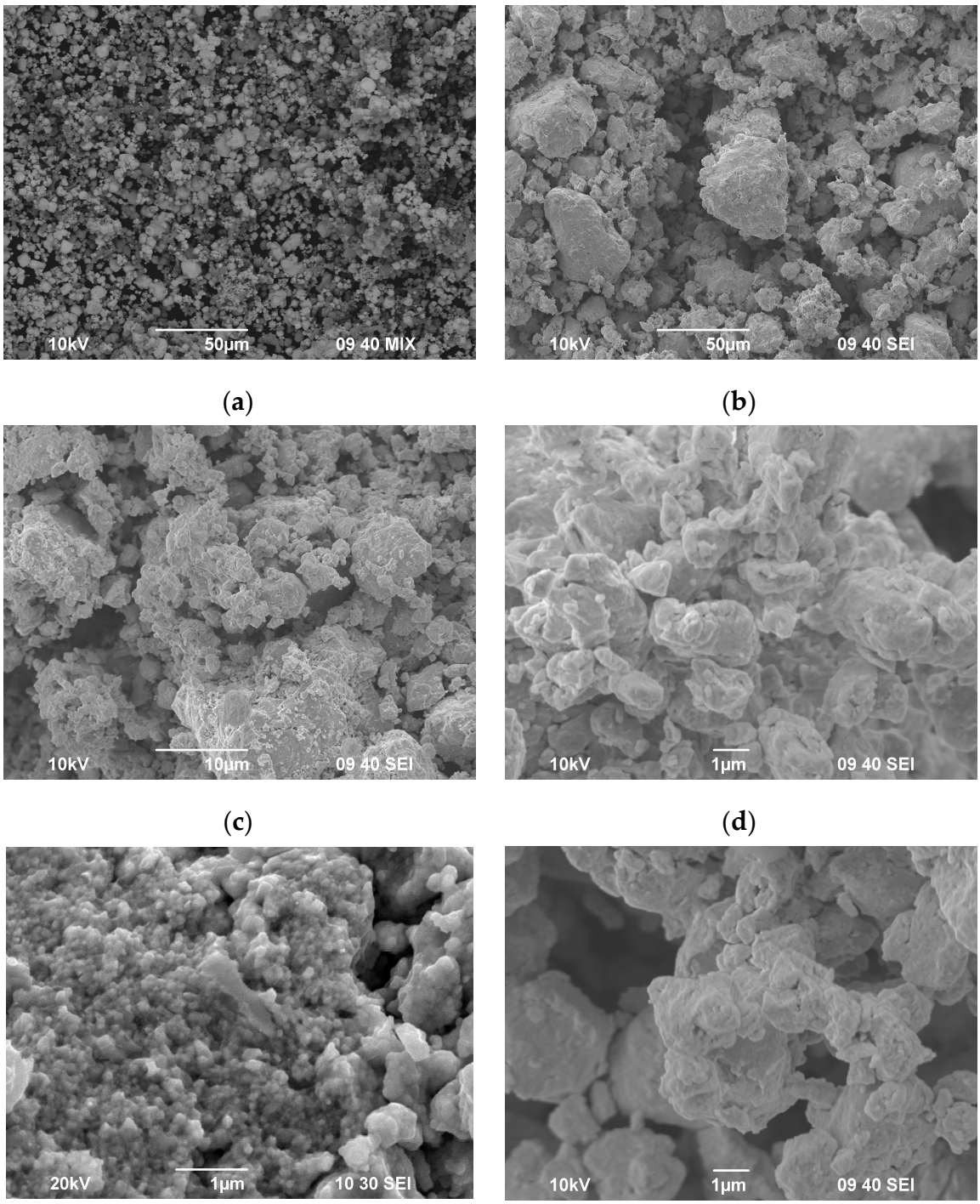

Figure 3. SEM images of W-7%Ni-3%Fe powder agglomerates for different HEBM: times (**a**) 0 min; (**b**) 5 min; (**c**) 10 min; (**d**) 20 min; (**e, f**) 40 min.

Preprints (www.preprints.org) | NOT PEER-REVIEWED | Posted: 18 April 2023 doi:10.20944/preprints202304.0503.v1

As one can see in the images presented in Fig. 3, large enough micron-sized agglomerates consisting of several tens nanoparticles having splinter shapes (Fig. 4a) or round one (Fig. 4b) form in the course of HEBM.

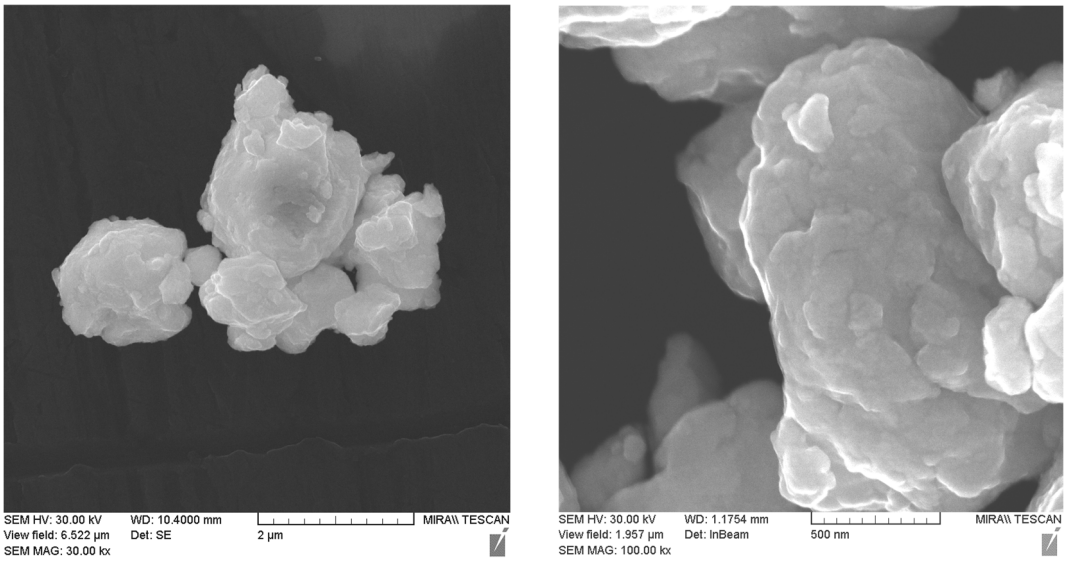

(a) **(b)**

Figure 4. SEM images of the nanoparticles in the powder agglomerates 90%W-7%Ni-3%Fe for different HEBM times: (**a**) t_{HEBM} = 10 min; (**b**) t_{HEBM} = 40 min.

The results of the XRD phase analysis shows the decrease in the intensity and broadening of the XRD peaks of α-W to take place in the course of HEBM (Fig. 5a). No peaks corresponding to iron and nickel were visible in the XRD curves. It allows suggesting a strong fragmentation of the Ni and Fe particles to take place during HEBM.

A shift of the tungsten peaks towards greater diffraction anglers was observed (Fig. 5b). The (110) α-W peak position in the initial coarse-grained powder corresponds to the diffraction angle $2\Theta_{max} = 40.26^{o} \pm 0.02^{o}$. After MA during t_{HEBM} = 40 min, the (110) α-W XRD peak shifted by ~0.08-0.12^{o} up to $2\Theta_{max} = 40.34\text{-}40.38^{o}$. According to Wulff-Bragg's equation ($2d_{hkl} = n\lambda_{Cu}\cdot\sin 2\Theta_{hkl}$), this evidences the compressive internal stress fields to form in the tungsten nanoparticles in the course HEBM that leads to a decrease in the interplanar distances d_{hkl}.

Preprints (www.preprints.org) | NOT PEER-REVIEWED | Posted: 18 April 2023 doi:10.20944/preprints202304.0503.v1

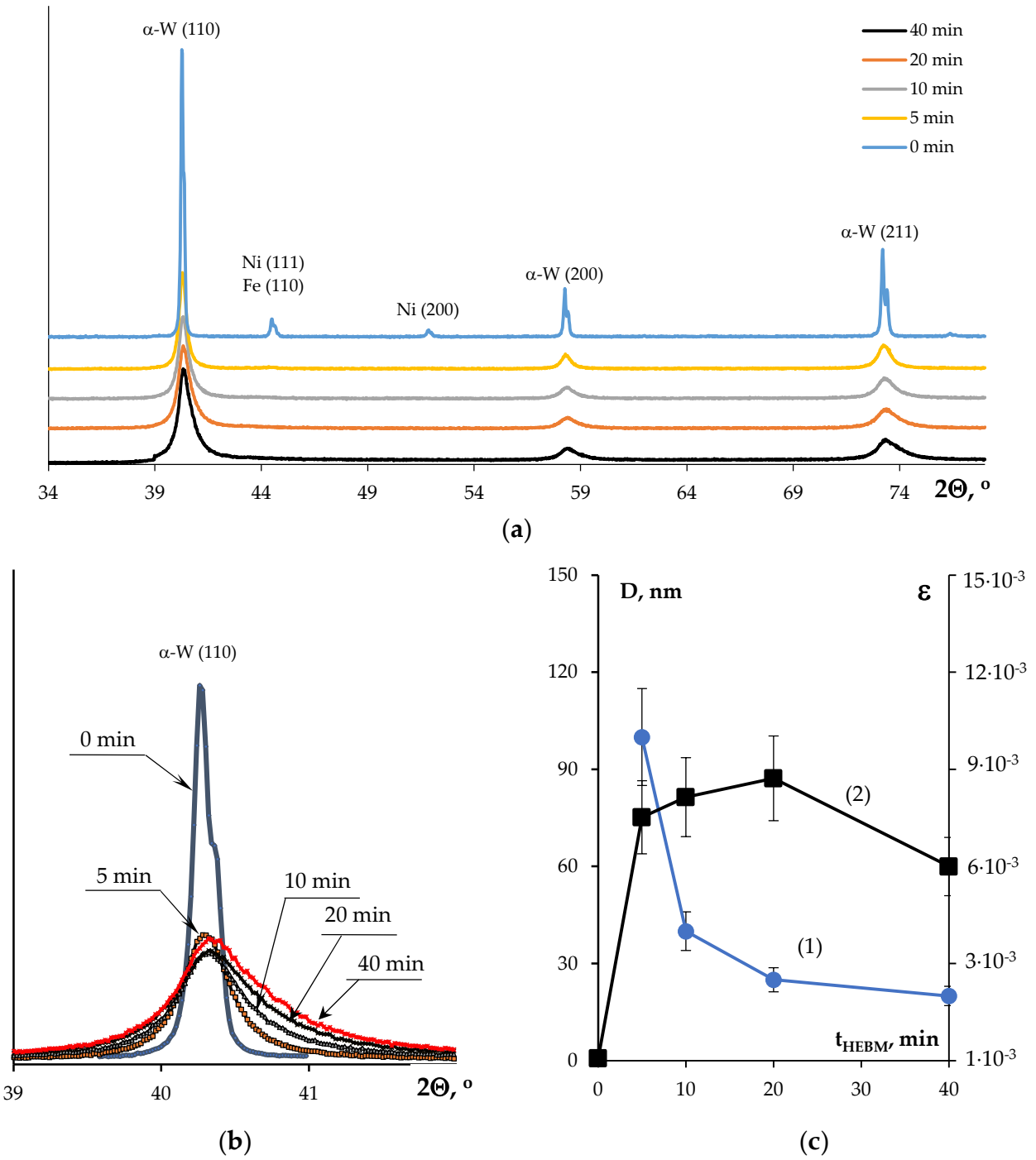

Figure 5. Results of XRD phase analysis of the powders 90%W-7%Ni-3%Fe: (**a**) overview XRD curves after different HEBM times; (**b**) effect of the HEBM time on the broadening of the (110) α-W pears [45]; (**c**) effect of the HEBM time on the CSR size (1) and on the magnitude of the micro strain of the α-W crystal lattice (2) [45].

Note that one can see an asymmetry of the tungsten XRD peaks in Fig. 5b – the (110) α-W peaks are broadened stronger towards greater diffraction angles 2Θ. After HEBM during 40 min, the half width at half maximum (HWHM) of the (110) α-W peak at small diffraction angles was $\Theta_{-0.5}$ ~ 0.30-0.32° whereas the one at large diffraction angles $\Theta_{-0.5}$ ~ 0.42-0.44°. In the initial state, the (110) α-W peaks were highly symmetric ($\Theta_{-0.5}$ ~ $\Theta_{+0.5}$ ~ 0.06-0.10°). According to [45], this result means that the nanoparticles after HEBM have a core-shell structure – a strain-induced dissolving of nickel and iron atoms in the surface layers of the α-W nanoparticles takes place during HEBM. It leads to the formation of the internal compressive stress fields in the surface layers of the α-W nanoparticles and, as a consequence, to the broadening of the α-W peaks towards greater diffraction angles.

Preprints (www.preprints.org) | NOT PEER-REVIEWED | Posted: 18 April 2023 doi:10.20944/preprints202304.0503.v1

The calculations of the coherent scattering region sizes (D_{XRD}) according to Williamson-Hall model shows D_{XRD} to decrease from ~80-100 nm down to ~20-25 nm with increasing t_{HEBM} from 5 up to 40 min. The estimates obtained evidence the agglomerates shown in Fig. 3 to consist of several tens or hundred tungsten particles in average.

It is worth to pay attention to a non-monotonous character of the dependence of the micro strain of the tungsten crystal lattice (ε) calculated according to Williamson-Hall method on the HEBM time. As one can see in Fig. 5c, the maximum value $\varepsilon_{max} \sim 9 \cdot 10^{-3}$ was achieved after 20 min of HEBM. At further increasing of the HEBM time, the magnitude of ε decreased down to $\sim 6 \cdot 10^{-3}$. So far, one can conclude essential compressive internal stress fields to form in the tungsten nanoparticles in the course of HEBM that leads to a strong distortion of the α-W crystal lattice (see [51]).

The investigations of the chemical composition have shown that the oxygen concentration in the nanopowders after HEBM reached 1.5-1.55%. These results agree qualitatively with the ones of [52] where an increase in the oxygen concentration in the tungsten powders after HEBM was observed also. After annealing in hydrogen at 900 °C (1 h), the oxygen concentration in the nanopowders decreased down to 0.8-0.95%. The parameters of the XRD peaks of α-W did not change after annealing in hydrogen.

3.2. Sintering the nanopowders in hydrogen

The investigations of the macrostructure of the samples have shown that the sintering of the nanopowders at 1450 at 1500 °C leads to formation of large pores (Fig. 6). This leads to a decrease in the density of the samples sintered from the mechanically activated nanopowders (Table 3). Sintering at lower temperatures (1250, 1300, and 1350 °C) did not result in formation of the macropores. No macropores were observed when sintering the coarse-grained powders.

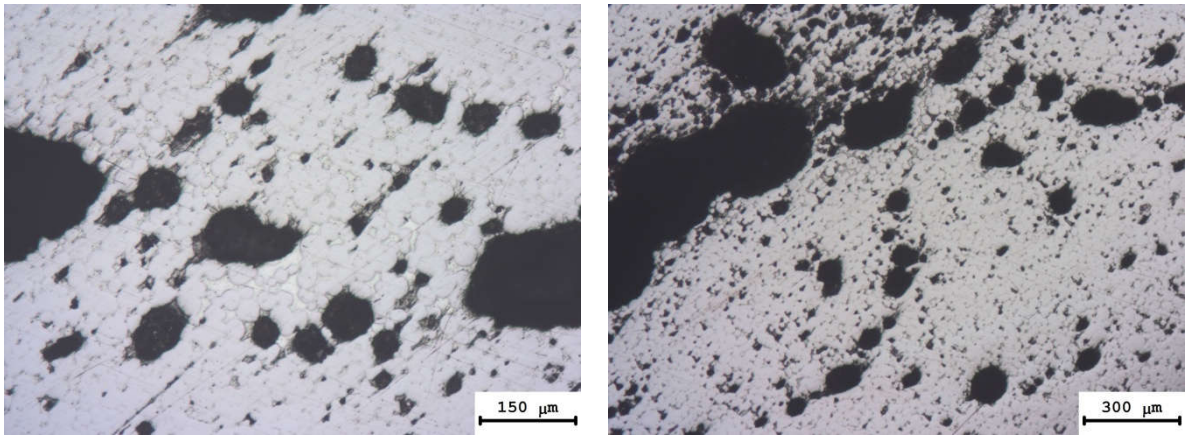

(**a**) (**b**)

Figure 6. Appearance of the W-7%Ni-3%Fe alloy samples sintered in hydrogen from the nanopowders obtained by HEBM. Sintering temperature: (**a**) 1450 °C; (**b**) 1500 °C.

The chemical reaction of hydrogen with oxygen adsorbed on the nanopowder particle surfaces is the most probable origin of the macropore formation. This reaction goes with formation of water vapor: $2H_2 + O_2 = 2H_2O$ (see [53]). The removing of the water vapor from the nanopowders pressed in advance is difficult that leads to an increase in the gas pressure inside the micropores and, as a consequence, to the formation of large macropores at elevated temperatures. The second factor promoting the macropore formation can be more intensive diffusion of hydrogen in the nanostructured HTAs. The investigations of the chemical composition have shown the hydrogen concentration in the samples sintered from the nanopowders reaches 83-97 ppm (T_s = 1450-1500 °C) while in the samples sintered from the coarse-grained powders, the hydrogen concentration varied from 2.6 to 11 ppm.

Preprints (www.preprints.org) | NOT PEER-REVIEWED | Posted: 18 April 2023 doi:10.20944/preprints202304.0503.v1

Table 2 presents the results of investigations of the density and mean grain sizes for the W-7%Ni-3%Fe alloy samples sintered in hydrogen at different temperatures. Fig. 7 presents the microstructure of the HTA samples sintered in hydrogen from the coarse-grained powders and nanopowders.

Table 2. Microstructure characteristics and mechanical properties of the W-7%Ni-3%Fe alloy samples obtained from the nanopowders by sintering in hydrogen.

	Characteristics of alloy obtained from coarse-grained powders							Characteristics of alloy obtained from nanopowders						
T_s, °C	ρ, g/cm³	d, μm	σ_0, MPa	σ_y, MPa	Hv, GPa	Ys, MPa	H, mm	ρ, g/cm³	d, μm	σ_0, MPa	σ_y, MPa	Hv, GPa	Ys, MPa	H, mm
1250	17.94	5-10	520	1150	4.2	1830	3.8	17.79	1-3	960	1540	7.9	1900	5.1
1300	18.02	~5-10	460	990	4.2	1700	4.15	17.93	1-3	1000	1340	7.5	2050	4.68
1350	18.06	~10	290	790	4.1	1650	4.23	17.95	1-3	860	1200	7.2	1870	3.72
1400	18.14	~20	230	740	4.0	1640	4.05	17.49	3-5	300	740	6.9	1500	3.1
1450	18.11	40-45	220	600	3.8	1590	3.7	17.05 [1]	~10	-	-	6.5	-	-
1500	18.06	~50	200	690	3.6	1580	3.2	16.87 [1]	~22	-	-	6.2	-	-

[1] The density was measured by measuring the mass and geometrical sizes of the samples.

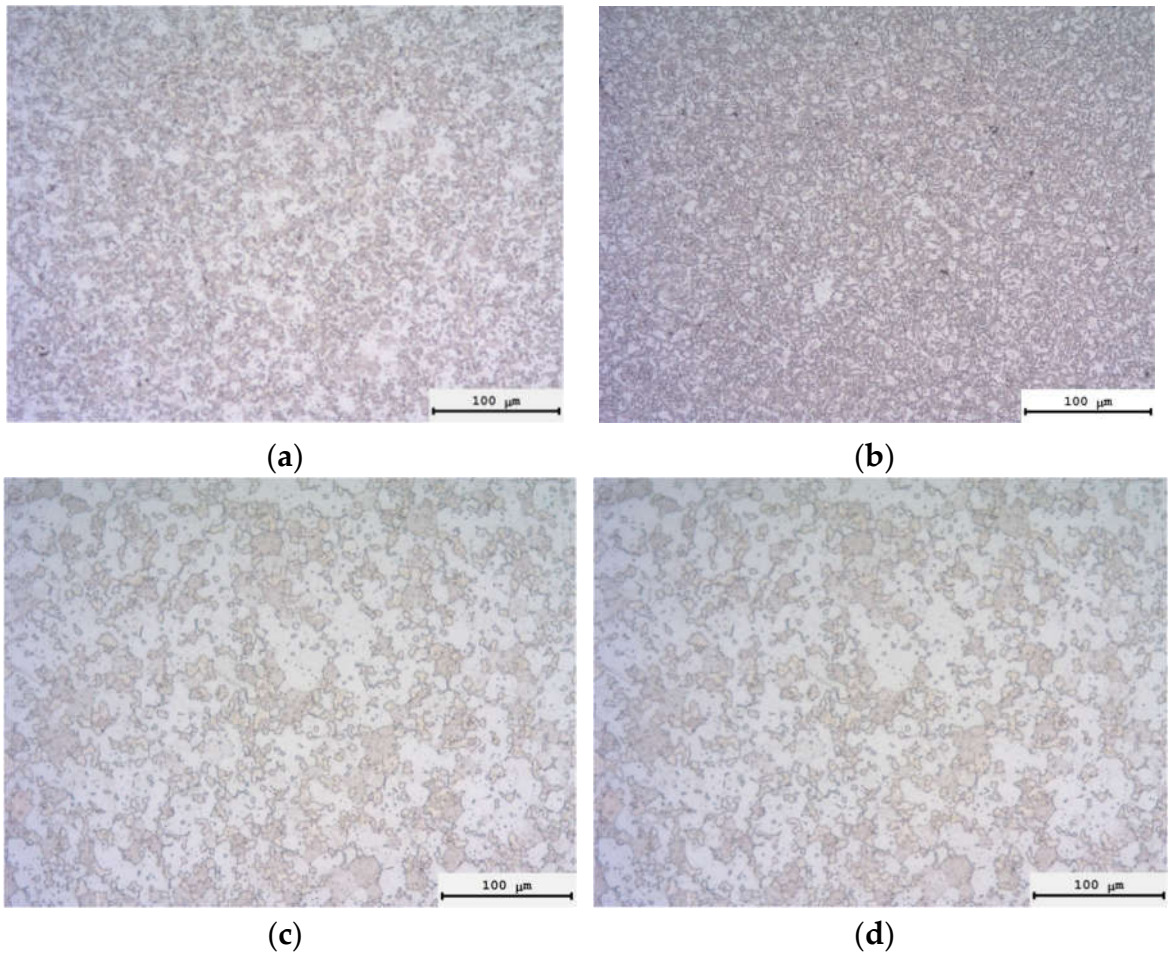

Figure 7. Microstructure of W-7%Ni-3%Fe alloy sintered from coarse-grained (**a**, **c**, **e**) and nanopowder (t_{HEBM} = 20 min) (**b**, **d**, **f**). Sintering temperature T_s = 1250 °C (**a, b**), 1400 °C (c, **d**).

The analysis of the results presented shows the increasing of the sintering temperature up to 1250 and 1400 °C to result in a smooth increase in the mean tungsten particle sizes up to ~1 μm and ~3-5 μm, respectively (Fig. 7b, d). The mean grain sizes in the samples sintered from the nanopowders were less than the ones in the samples sintered from the coarse-grained powders but the alloy microstructure was nonuniform enough.

Preprints (www.preprints.org) | NOT PEER-REVIEWED | Posted: 18 April 2023 doi:10.20944/preprints202304.0503.v1

The macroscopic inhomogeneities of the specimen microstructure were observed at the initial stages of sintering at the sintering temperatures 1150-1200 °C (Fig. 8a, b). The presence of such inhomogeneities may be caused by the presence of large agglomerates in the nanopowders after HEBM. The degree of the structure inhomogeneity decreases with increasing sintering temperature (Fig. 8c).

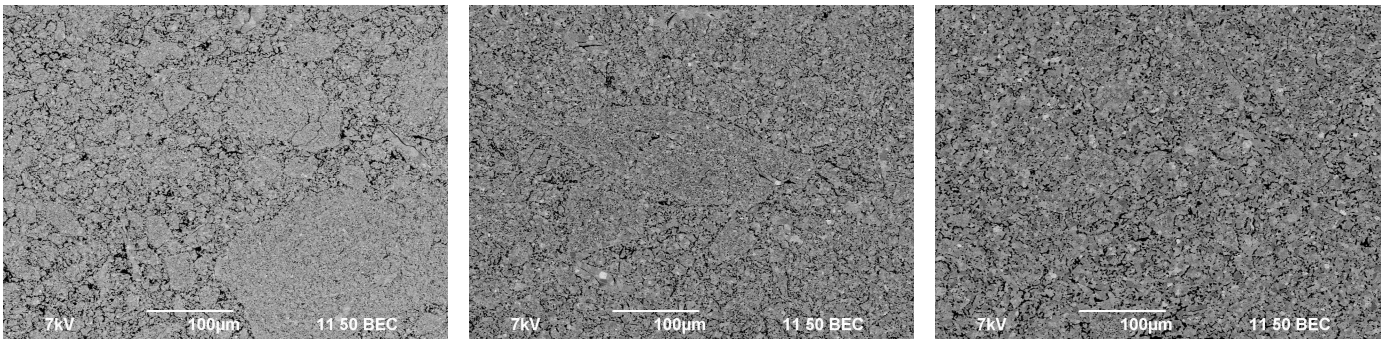

(**a**) (**b**) (**c**)

Figure 8. Microstructure of the W-7%Ni-3%Fe alloy sintered from the nanopowder (t_{HEBM} = 20 min) at the temperatures 1150 °C (**a**), 1200 °C (**b**), and 1400 °C (**c**).

The XRD phase analysis results shows the increasing of the sintering temperature to result in an increase in the intensity of the α-W XRD peaks; the asymmetry and the broadening of the peaks decrease essentially.

The increase in the mean grain sizes with increasing HTA sintering temperature from 1250 °C up to 1400 °C leads to worsening of the mechanical properties of the alloy – the hardness decreased from 7.9 down to 6.9 GPa, the macroelasticity stress – from 960 down to 300 MPa, and the yield strength – from 1370 down to 620 MPa. Note that the mechanical properties of the samples sintered from the nanopowders at T_s = 1250 and 1300 °C were better considerably than the ones of the samples sintered from the coarse-grained powders (Table 2). Further increasing of the annealing temperature (over 1350 °C) leads to a considerable decrease in the differences in the mechanical characteristics of the samples sintered from the coarse-grained and nanopowders.

3.3. Spark Plasma Sintering

Fig. 9 presents the temperature curves of the shrinkage (Fig. 9a, b) and the ones of the shrinkage rate (Fig. 9c, d) of the nanopowders. Table 3 presents the results of investigations of the microstructure, density, and mechanical properties of these ones.

Preprints (www.preprints.org) | NOT PEER-REVIEWED | Posted: 18 April 2023 doi:10.20944/preprints202304.0503.v1

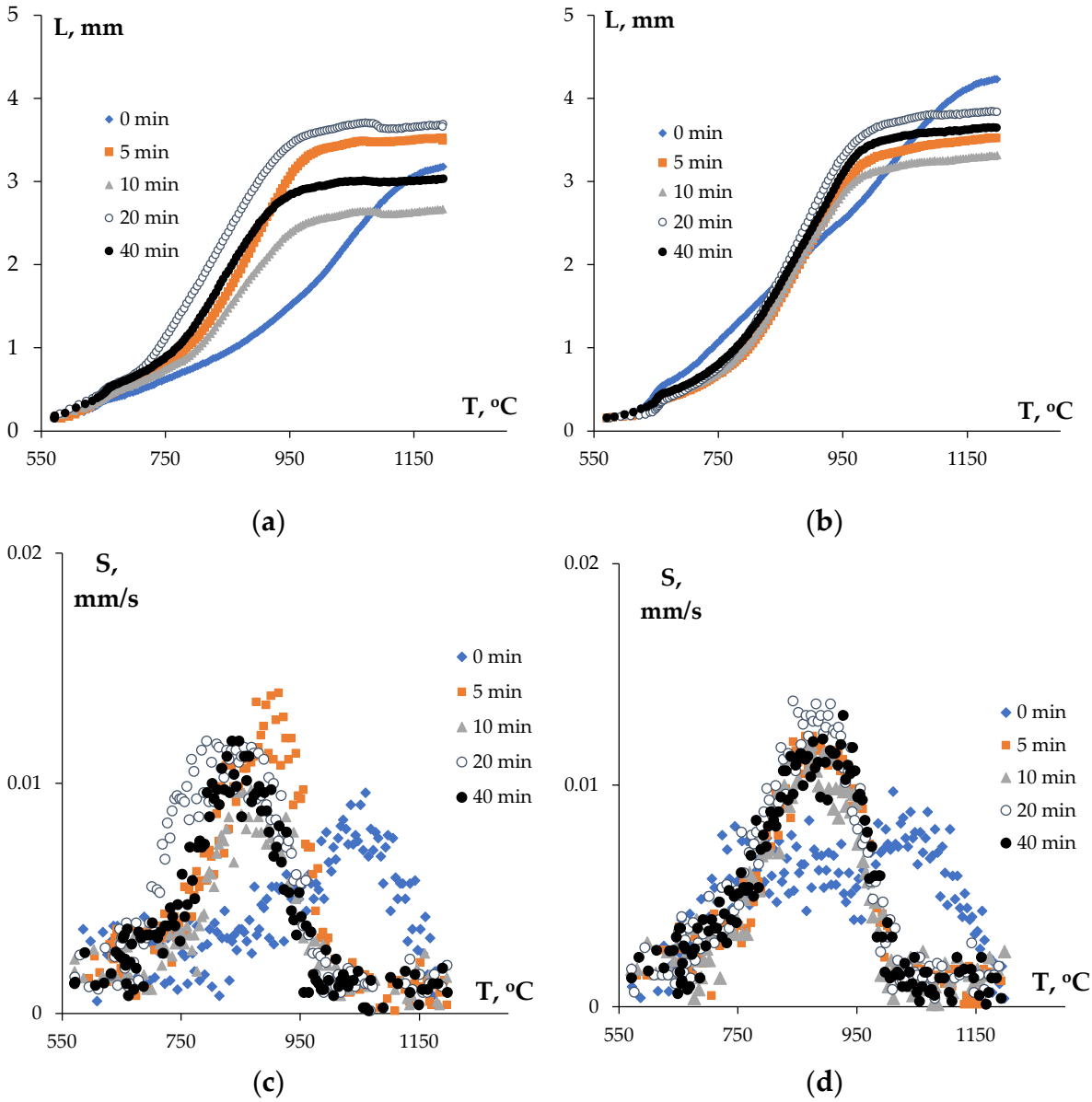

Figure 9. Temperature curves of shrinkage (**a**, **b**) and shrinkage rate (**c**, **d**) for the W-7%Ni-3%Fe nanopowders after HEBM (**a**, **c**), and after HEBM and annealing in hydrogen (**b**, **d**).

Table 3. Microstructure characteristics and mechanical properties of the W-7%Ni-3%Fe alloy samples obtained by SPS from nanopowders (T_s = 1200 °C).

	Characteristics of alloy obtained from non-annealed nanopowders							Characteristics of alloy obtained from annealed nanopowders						
t_{HEBM}, min	ρ, g/cm³	d, μm	σ_0, MPa	σ_y, MPa	H_v, GPa	Y_s, MPa	H, mm	ρ, g/cm³	d, μm	σ_0, MPa	σ_y, MPa	H_v, GPa	Y_s, MPa	H, mm
0	16.97	1.3	920	1850	4.2	-	4.9	17.02	1.2	1050	1930	4.3	-	5.1
5	16.64	0.9	1330	2160	4.5	2280	5.8	16.79	1.0	1400	2270	4.8	2350	5.1
10	16.45	0.8	1450	2180	4.7	-	5.7	16.92	0.7	1520	2310	4.9	-	5.4
20	15.68	0.7	1500	2370	4.8	-	5.7	16.31	0.6	1610	2350	5.3	-	6.6
40	16.78	0.7	1480	2350	4.7	2480	5.6	17.04	0.6	1530	2320	4.9	2630	6.1

The analysis of the curves L(T) presented in Fig. 9a shows the intensive shrinkage of the nanopowders to begin at lower temperatures as compared to the initial coarse-grained powders. The increasing of the HEBM time from 5 up to 20 min leads to a shift of the temperature of beginning of the intensive shrinkage stage from ~780-800 °C down to ~720 °C with simultaneous increase in the

Preprints (www.preprints.org) | NOT PEER-REVIEWED | Posted: 18 April 2023 doi:10.20944/preprints202304.0503.v1

maximum shrinkage L_{max} from ~2.6-2.7 mm up to 3.6-3.7 mm. The temperature of the end of the intensive shrinkage stage increases weakly with increasing t_{HEBM} from 5 up to 20 min. Further increasing of the HEBM time up to 40 min leads to an increasing of the temperature of beginning of the intensive shrinkage stage up to ~750 ^{o}C and to decreasing of L_{max} down to ~3.0-3.1 mm. Similar character of the dependence $L_{max}(t_{HEBM})$ was observed for the annealed nanopowders (Fig. 9b).

As one can see in Fig. 9b, the increasing of the HEBM time leads to a shift of the curve S(T) towards lower temperatures and to an increase in the maximum shrinkage rate S_{max}. As one can see in Fig. 9b, the maximum shrinkage rate for the coarse-grained powders was observed at the temperatures ~1060-1080 ^{o}C; the shrinkage rate at that was S_{max} ~10^{-2} mm/s. The increasing of the HEBM time up to 20-40 min leads to increasing of S_{max} up to ~(1.1-1.2) 10^{-2} mm/s and to decreasing of the temperature corresponding to the maximum of the curve S(T) up to 850-890 ^{o}C. In the case of the annealed nanopowders, the maximum shrinkage rate S_{max} ~(1.3-1.4) 10^{-2} mm/s was observed at the sintering of the nanopowders subjected HEBM for 20 min.

The annealing in hydrogen affects the curves L(T) essentially and, to less extent, the curves S(T). Comparing Fig. 9a and Fig. 9b shows the annealing in hydrogen to result in an increasing of the shrinkage of the initial coarse-grained powders. The scale of increasing of the maximum shrinkage L_{max} for the annealed nanopowders was ~0.1-0.15 mm and depended on the HEBM time weakly. The annealing of the nanopowders in hydrogen leads to an insufficient decrease in the temperature corresponding to the maximum of the curve S(T) and to weak increasing of the maximum shrinkage rate S_{max}.

It is interesting to note that the densities of the samples depend on the HEBM time non-monotonously. As one can see from Table 3, the increasing of t_{HEBM} from 0 up to 20 min leads to a decrease in the density from 16.97 down to 15.68 g/cm^3. After HEBM for 40 min, the densities of the samples increased up to 16.78 g/cm^3. The dependence of density on the HEBM time for the samples sintered from the annealed nanopowders has similar character. It should be stressed here that the annealing resulted in an increase in the densities of the sintered samples in ~0.1-0.2 g/cm^3.

The analysis of the results presented in Table 4 shows the increasing of the HEBM time leads to a decrease in the mean grain sizes in the alloys sintered at 1200 ^{o}C. The mean grain sizes in the alloys sintered from the annealed and non-annealed powders were close to each other (Fig. 10).

Preprints (www.preprints.org) | NOT PEER-REVIEWED | Posted: 18 April 2023 doi:10.20944/preprints202304.0503.v1

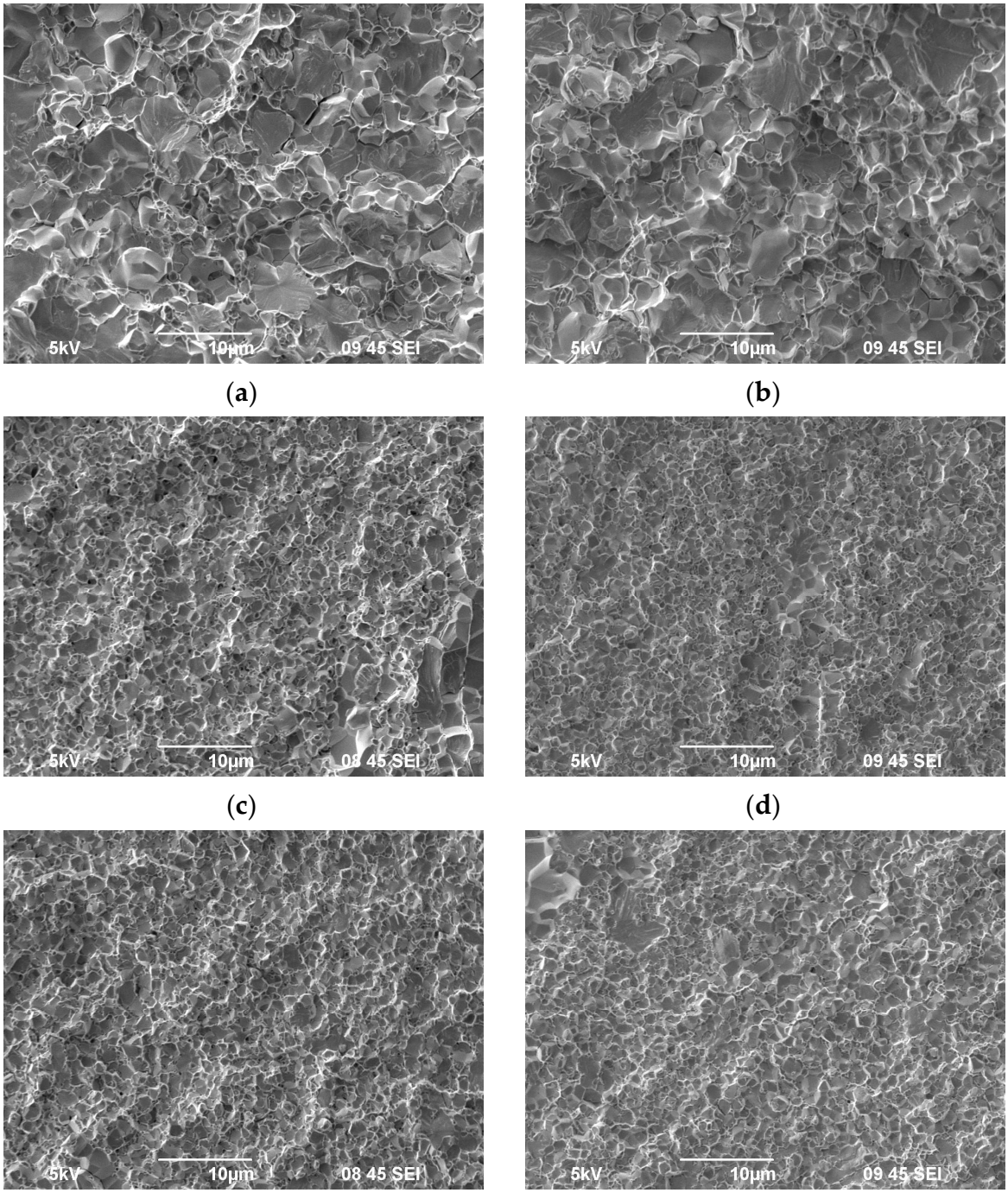

Figure 10. Microstructure of the W-7%Ni-3%Fe alloy obtained by SPS at 1200 °C from non-annealed (**a, c, e**) and annealed (**b, d, f**) nanopowders. HEBM time: (**a, b**) 0 min; (**c, d**) 10 min; (**e, f**) 40 min.

The HTAs obtained by SPS have a uniform enough microstructure (Fig. 10, 11), which few large grains are present in. These grains are the recrystallized microstructure areas with minimal γ-phase content (Fig. 11). Such large grains were observed in the samples obtained from the nanopowders with $t_{HEBM} \geq 10$ min most often. The volume fraction and sizes of the abnormally large grains in the samples sintered from the annealed nanopowders were smaller considerably than the ones in the samples sintered form the non-annealed nanopowders (Fig. 10). This result allows suggesting the presence of the agglomerates after HEBM and increased oxygen concentration in the nanopowders to be the most probable origins of the appearing of the abnormally large grains.

Preprints (www.preprints.org) | NOT PEER-REVIEWED | Posted: 18 April 2023 doi:10.20944/preprints202304.0503.v1

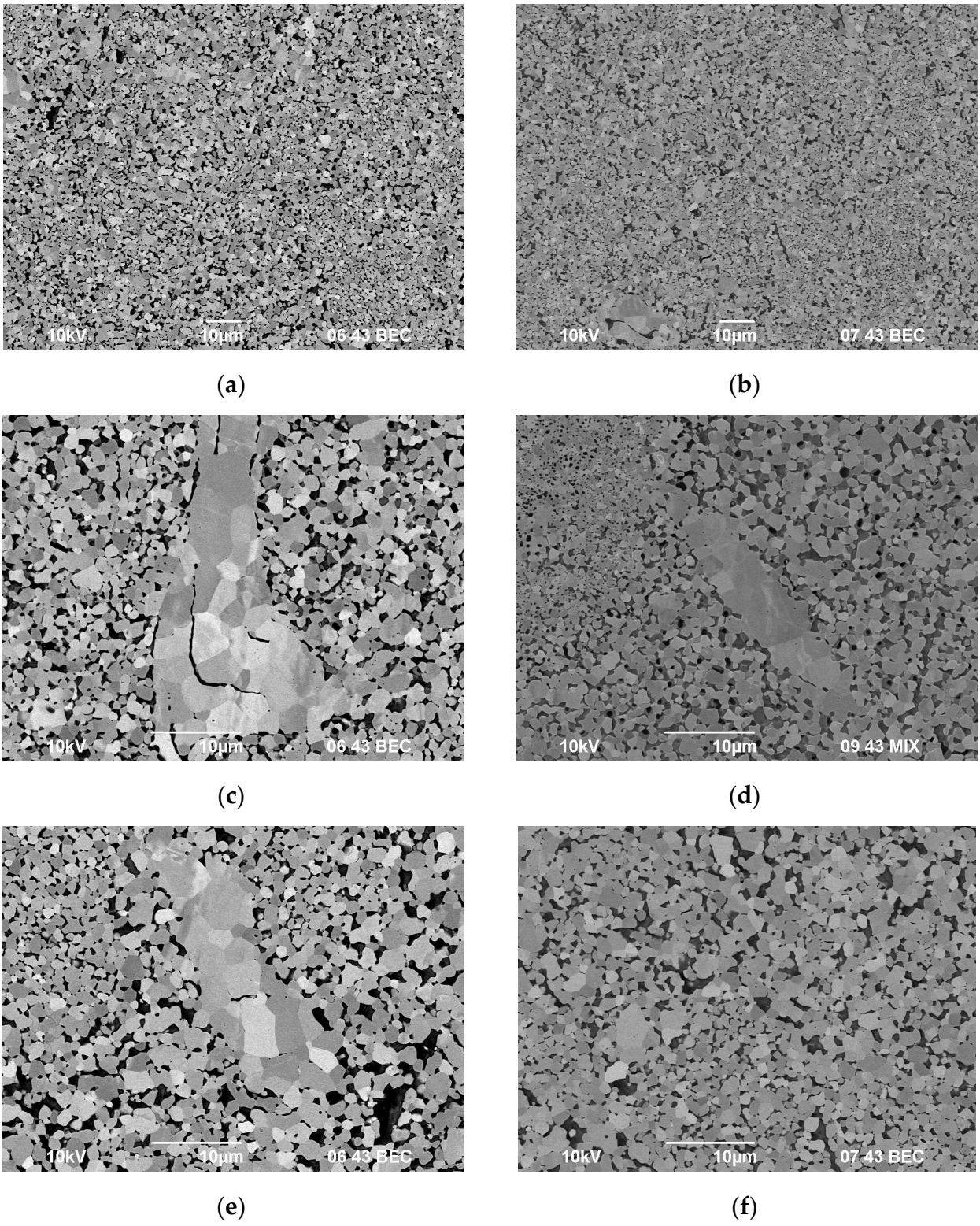

Figure 11. Microstructure of the samples obtained by SPS from the annealed (**a**) and non-annealed (**b**) nanopowders after HEBM (t_{HEBM} = 40 min). The areas with the abnormally large grains in the microstructure of the W-7%Ni-3%Fe alloy obtained by SPS at 1200 °C from non-annealed (**c, d, e**) and annealed (**f**) nanopowders: (**c**) t_{HEBM} = 10 min, (**d**) t_{HEBM} = 20 min; (**e, f**) t_{HEBM} = 40 min.

Fig. 12 presents the results of XRD phase analysis of the samples obtained by SPS from the nanopowders. The analysis of the XRD curves presented shows the broadening of the α-W peaks in the sintered samples to be much lower than the one in the nanopowders after HEBM. The asymmetry of the α-W XRD peaks in the sintered samples was absent while the peak positions $2\Theta_{max}$ was shifted

Preprints (www.preprints.org) | NOT PEER-REVIEWED | Posted: 18 April 2023 doi:10.20944/preprints202304.0503.v1

towards smaller diffraction angles as compared to the one in the nanopowder. No essential differences in the characteristics of the (110) α-W peaks for the samples sintered from the nanopowders subjected to HEBM of different times were observed (Fig. 12b, 12c). This evidences the intragranular stresses formed in the tungsten powders during HEBM to relax in the course of sintering.

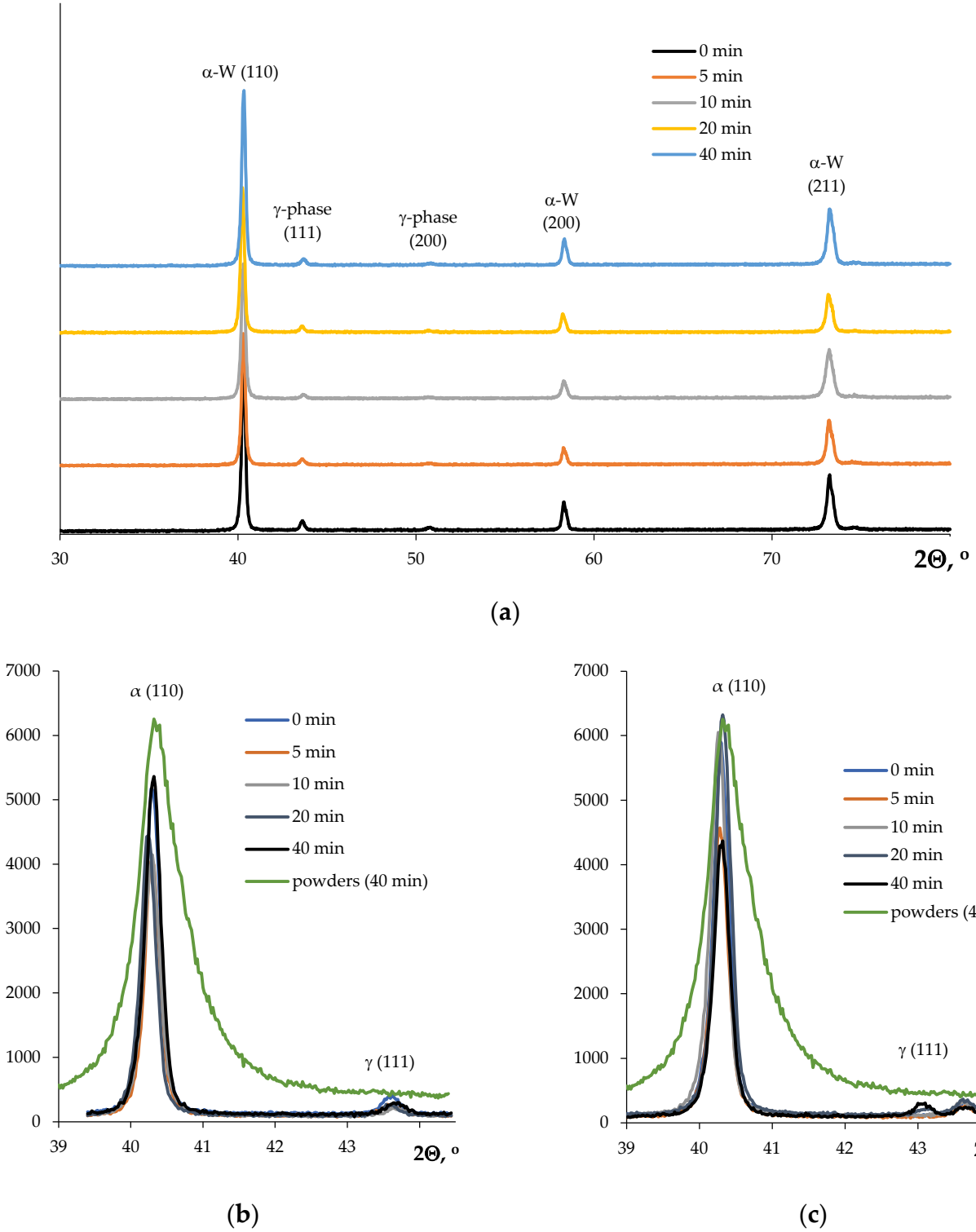

Figure 12. Results of XRD analysis of the W-7%Ni-3%Fe alloy obtained by SPS at 1200 °C. Effect of the HEBM time on the parameters of the (100) α-W peak in the samples sintered from the non-annealed (**a**) and annealed nanopowders (**b**).

Preprints (www.preprints.org) | NOT PEER-REVIEWED | Posted: 18 April 2023 doi:10.20944/preprints202304.0503.v1

The low-intensity γ-phase peaks are visible in the XRD curves of the sintered samples. Such peaks were absent in the XRD curves of the nanopowders after HEBM (Fig. 12b, c). The characteristics of the XRD peaks from the γ-phase almost do not depend on the HEBM time (Fig. 12b, c).

4. Discussion

The nonmonotonous dependence of the density of the samples obtained by SPS on the HEBM time (Fig. 13) is one of the most interesting results obtained in the present work. The decrease in the alloy density from 98.4% down to 90.9% for the samples sintered from the non-annealed nanopowders and from 98.7% down to 94.6% for the ones sintered from the annealed nanopowders was observed when increasing HEBM time from 0 up to 20 min.

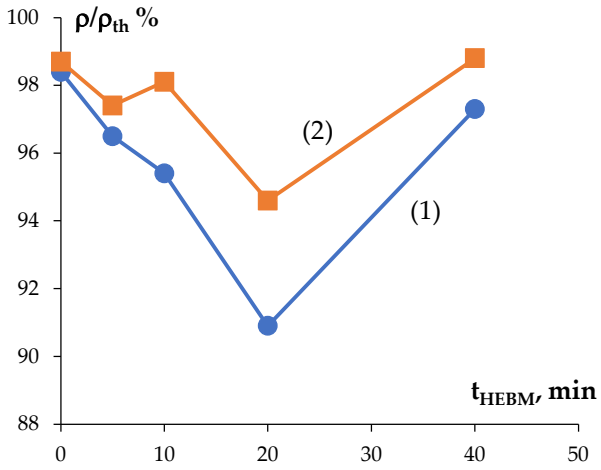

Figure 13. Dependencies of relative density of the W-7%Ni-3%Fe alloy sintered at 1200 °C on the HEBM time: (1) – densities of the samples sintered from the non-annealed nanopowders; (2) – densities of the samples sintered from the annealed nanopowders.

Note that large pores were absent in the microstructure of the sintered samples. The comparison of the microstructure of the samples sintered from the coarse-grained powders and from the nanopowders after t_{HEBM} = 20 min (Fig. 8, 9) did not reveal any essential increase in the sizes and volume fraction of the pores. So far, one can conclude that the decrease in the density of the alloy sintered from the nanopowders originates not from the increase in the volume fraction of the pores but from other factors. This conclusion is supported indirectly by the analysis of the curves L(T) and S(T) presented in Fig. 7. As it has been shown above, the maximum values of the shrinkage L_{max} and of the shrinkage rate S_{max} were observed in the case of SPS of the powders subjected to HEBM for 20 min.

To answer the question of the origin of the non-monotonous dependence of the density on the HEBM time, let us analyze the SPS mechanisms of the W-Ni-Fe nanopowders. First, it is worth noting that the characteristic sintering temperature T_s = 1200 °C is ~0.4$T_{m(W)}$ and, according to [54], the diffusion intensity and the strain rate in tungsten are very low. (Here $T_{m(W)}$ = 3695 K is the melting point of tungsten [54]).

As one can see in Fig. 9a, b, the curve L(T) has usual three-stage character: the shrinkage of the nanopowders is finished almost completely within the intensive shrinkage stage (Stage II) in the temperature range from 750-800 °C to 1000-1050 °C. The intensity of shrinkage of the nanopowders within the third stage of sintering (T_s > 1000-1050 °C), which the grain growth occurs at often is very low.

The analysis of the compaction kinetics of the nanopowders at Stage II can be made using Young-Cutler model [55] developed for the analysis of the compaction curves of the fine-grained powders in the continuous heating regime. The Young-Cutler model [55] describes the initial stage of non-isothermic sintering of spherical particles in the conditions of simultaneous volume and grain

Preprints (www.preprints.org) | NOT PEER-REVIEWED | Posted: 18 April 2023 doi:10.20944/preprints202304.0503.v1

boundary diffusion as well as plastic deformation processes. According to [55], the slope of the dependence $\ln(T\partial\varepsilon/\partial T) - T_m/T$ corresponds to the effective activation energy of the non-isothermic sintering process mQ_{s2} where m is a numerical coefficient depending on the diffusion mechanism, $T_m = T_{m(Ni)} = 1723$ K is the melting point of the γ-phase [1, 2]. The magnitude of $m = 1/3$ for the case of the grain boundary diffusion, $m = 1/2$ for the case of the volume diffusion in the crystal lattice, $m = 1$ for the case of the creep of the material [55].

The dependencies $\ln(T\cdot\partial\varepsilon/\partial T) - T_m/T$ are presented in Fig. 14. As one can see in Fig. 14, the dependencies $\ln(T\cdot\partial\varepsilon/\partial T) - T_m/T$ have usual two-stage character that confirms the correctness of application of the Young-Cutler model to analyze the sintering kinetics of the W-Ni-Fe alloy. The values of the effective sintering activation energy at the intensive shrinkage stage (mQ_{s2}) are presented in Table 4. The mean uncertainty of determining the activation energy mQ_{s2} was ±0.2 kT_m.

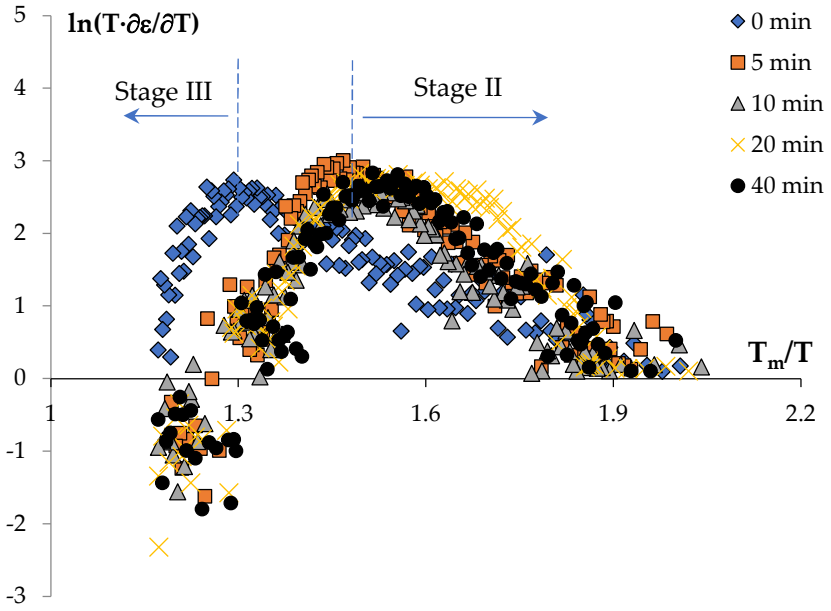

Figure 14. Dependencies $(T\cdot\partial\varepsilon/\partial T) - T_m/T$ for the W-7%Ni-3%Fe alloy. Analysis of the compaction mechanisms of the non-annealed nanopowders at Stage II.

Table 4. SPS activation energies of nanopowders W-7%Ni-3%Fe

	Nanopowders after HEBM				Nanopowders after HEBM and annealing in hydrogen			
	Stage II		Stage III		Stage II		Stage III	
t_{HEBM}, min	mQ_{s2}, kT_m	m	Q_{s2}, kT_m / kJ/mol	Q_{s3}, kT_m / kJ/mol	mQ_{s2}, kT_m	m	Q_{s2}, kT_m / kJ/mol	Q_{s3}, kT_m / kJ/mol
0	3.9	1/3	11.7 / 167	16.1 / 230	3.2	1/3	9.6 / 137	17.2 / 246
5	6.5		6.5 / 93	17.8 / 255	5.9		5.9 / 84	15.4 / 221
10	6.0	1	6.0 / 86	19.1 / 273	4.9	1	4.9 / 70	14.7 / 210
20	5.2		5.2 / 75	18.9 / 271	4.6		4.6 / 65	15.8 / 226
40	7.0		7.0 / 100	19.2 / 275	6.4		6.4 / 92	16.8 / 240

In the case of the coarse-grained powders, the magnitude of the effective SPS activation energy mQ_{s2} was close to the activation energy of the grain boundary diffusion in nickel ($Q_{b(Ni)} = 115$ kJ/mol [54]) at $m = 1/3$. This allows suggesting the kinetics of high-speed sintering of the coarse-grained powders W-7%Ni-3%Fe at the intensive shrinkage stage to be controlled by the intensity of the grain boundary diffusion in the γ-phase.

A good correspondence of the SPS activation energy of the nanopowders to the data on the activation energy of the diffusion processes reported in the literature was observed for $m = 1$ (Table

 doi:10.20944/preprints202304.0503.v1

4). The value of m = 1 allows concluding the sintering kinetics of the nanopowders W-7%Ni-3%Fe to be determined by the Coble creep intensity. This conclusion agrees qualitatively with M.F. Ashby deformation-mechanism maps [54], in which the SPS regimes used in the present work correspond well to the creep area for nickel (stress σ = 70 MPa ~ $9 \cdot 10^{-4} G$ where G = 78.9 GPa [54] is the shear modulus for nickel, temperature 1200 °C). In our opinion, large lengths of the grain boundaries in the sintered materials is the origin of the realization of Coble creep mechanism in SPS of nanopowders since no intensive grain growth takes place at this sintering stage yet. Note also that the decreasing of the grain sizes would lead to an essential increase in the creep rate in the metal materials [56]. Note also that Coble creep is one of main compaction mechanisms in SPS of WC [57], WC-Co [58,59], and YAG:Nd-W [60] nanopowders.

Note that sometimes lower values of the activation energy of the grain boundary diffusion in fine-grained nickel are reported in the literature as well. In particular, the creep activation energy of 110-115 kJ/mol and the activation energy of the grain boundary diffusion of ~66 kJ/mol were reported for ultrafine-grained nickel with the grain sizes 0.3-0.5 μm [61].

The annealing of the nanopowders in hydrogen leads to a decrease in the SPS activation energy (Table 4). In our opinion, it originates from, first of all, the reduced concentration of oxygen adsorbed on the nanopowder particle surfaces. This leads to an increase in the diffusion creep rate in the nanopowders W-7%Ni-3%Fe at elevated temperatures. Thin tungsten oxide layers, which can form on the W nanoparticle surfaces when heating in vacuum can be another origin of decrease in the creep rate. The oxide nanoparticles located at the tungsten grain boundaries can lead to a decrease in the creep rate at the second SPS stage.

In the high temperature range, the slope of the dependence $\ln(T \cdot \partial\varepsilon/\partial T) - T_m/T$ (Fig. 14) becomes negative. It means that one has to use another approach to estimate the sintering activation energy in the higher temperature range. According to [62], one can estimate the activation energy at this stage using the model of diffusion dissolving of pores located near the grain boundaries in the fine-grained materials. The correctness of application of this procedure was demonstrated earlier in [45,60,63,64]. The activation energy at the non-isothermic sintering stage Q_{s3} can be determined from the slope of the dependence $\rho(T)/\rho_{th}$ in the double logarithmic axes $\ln(\ln(\alpha \cdot \rho/\rho_{th}/(1-\rho/\rho_{th})) - T_m/T$ where α is the coefficient of compaction when pressing (α = 0.45 for nanopowders α-W) (Fig. 15). The mean uncertainty of determining the activation energy Q_{s3} was ±1.5 kT_m. The calculated values of Q_{s3} are presented in Table 4. For the annealed nanopowders, the value of Q_{s3} was ~2-3 kT_m less than the one for the mechanically activated nanopowders.

Preprints (www.preprints.org) | NOT PEER-REVIEWED | Posted: 18 April 2023 doi:10.20944/preprints202304.0503.v1

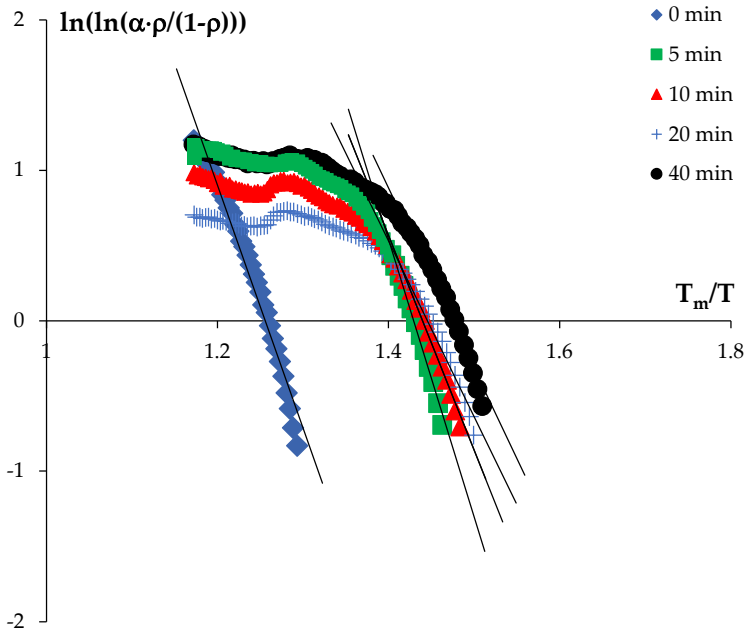

Figure 15. Dependencies $\ln(\ln(\alpha\cdot\rho/\rho_{th}/(1-\rho/\rho_{th}))$ – T_m/T for non-annealed nanopowders W-7%Ni-3%Fe.

The calculated values of the SPS activation energy correspond well to the activation energy of heterodiffusion of the tungsten atoms in the γ-phase (taking into account the corrections for the decrease in the activation energy of the grain boundary diffusion in the fine-grained materials [65]). Available data on sintering activation energies of W-Ni-Fe tungsten alloys give dramatically different values; Q_s for W-8.4Ni-3.6Fe alloy is 250 kJ/mol according to [66], whereas reference [67] gives Q_s = 367 kJ/mol for W-8.4Ni-3.6Fe alloy and 480 kJ/mol for 95W-3Ni-2Fe. In [68], the SPS activation energy for the fine-grained alloy W-5.6%Ni-1.4%Fe was shown to depend on the heating rate – at V < 30 °C/min the magnitude of Q_s = 454 kJ/mol, at V > 200 °C/min the magnitude of Q_s = 200 kJ/mol. The diffusion activation energy for ^{181}W in nickel crystal lattice is Q_v ~268-309 kJ/mol [8,69]. In the cases of the volume diffusion in the Ni-W system and in the γ-Fe-W one, the values of Q_v are 295-306 kJ/mol and 268 kJ/mol, respectively [70,71]. So far, one can conclude the compaction of the W-Ni-Fe nanopowders at high temperatures to be determined by the intensity of the heterodiffusion of the tungsten atoms in the crystal lattice of the γ-phase.

Summarizing the results of analysis, one should stress that the intensive shrinkage of the mechanically activated nanopowders W-7%Ni-3%Fe goes at low temperatures and is characterized by small values of compaction activation energy. In our opinion, low activation energy of sintering in nanopowder materials is the origin of the reduction of the activation energy of sintering of the W-Ni-Fe nanopowders.

According to the theory of the nonequilibrium grain boundaries [65], the increasing of the free (excess) volume of the grain boundaries Δα is the origin of the decrease in the activation energy of the grain boundary diffusion in the strongly deformed fine-grained metals and alloys. The magnitude of Δα is proportional to the density of orientation mismatch dislocations (OMDs) captured by the grain boundaries during severe plastic deformation. In the course of HEBM, the grinding of the γ-phase particles with the FCC lattice is difficult due to high ductility of these ones. In the course of HEBM, the grinding of the γ-phase particles and the accumulation of the OMDs at the grain boundaries take place [65]. The diffusion permeability of the γ-phase grain boundaries after HEBM appears to be higher than the one of "conventional" grain boundaries in the γ-phase formed during sintering individual γ-phase particles to each other. The enhanced diffusion permeability of the nonequilibrium grain boundaries to accelerated diffusion of the tungsten atoms in the γ-phase, and to enhanced Coble creep rate. These factors will lead to a decrease in the SPS activation energy of the nanopowders W-Ni-Fe.

Preprints (www.preprints.org) | NOT PEER-REVIEWED | Posted: 18 April 2023 doi:10.20944/preprints202304.0503.v1

The second factor promoting the decrease in the activation energy of the SPS of nanopowders can be the nonequilibrium state of their crystal lattice.

As it has been shown above, the asymmetric distortion of the (110) α-W XRD peak towards higher reflection angles after HEBM was observed. In our opinion, it means that the crystal lattice constant in the surface layers of the W particles appears to be smaller than the one in the central parts of the W particles. So far, the asymmetry of the (110) α-W XRD peak originates from the increase in the concentrations of the Ni and Fe atoms in the surface layers of the α-W particles. the concentrations of the Ni and Fe atoms in the surface layers of the α-W nanoparticles and from the increase in the concentration of the W atoms in the γ-phase particles with the nonequilibrium grain boundaries.

Tungsten is known to have a high solubility in nickel. At elevated temperatures, the concentration of the W atoms in the γ-phase can reach 25-28% [4]. Partial dissolving of the α-W nanopowders in the γ-phase takes place during sintering that leads to a decrease in the density of the sintered W-Ni-Fe samples. This process can be accelerated by larger specific surface area of the α-W nanoparticles, strong distortion of the crystal lattice in the surface layers of the α-W nanoparticles, and high diffusion permeability of the γ-phase nonequilibrium grain boundaries.

Now, let us consider the origins of the non-monotonous dependence of the density of the W-7%Ni-3%Fe alloy on the HEBM time (Fig. 13). This effect was observed, in particular, for the nanopowders annealed in hydrogen and, consequently, its nature is not related to the oxidation of the nanopowders in the course of storing.

The primary origin of the decrease in the alloy density is the strain-stimulated dissolving of the W atoms in the γ-phase lattice during HEBM. This effect can have a considerable scale for the W-7%Ni-3%Fe alloy since the volume fraction of the γ-phase in this alloy exceeds 20%. The increasing of the HEBM time lead to an increase in the volume fraction of the tungsten particles dissolved in the γ-phase. The decrease in the initial density of the W-Ni-Fe nanopowders would lead to a decrease in the final density of the alloy at given sintering regimes provided all other conditions being equal.

It is worth noting that the acceleration of the grain boundary diffusion processes and the increase in the creep rate should lead to an increase in the rate of solid phase sintering of the W-Ni-Fe nanopowders. This effect would compensate partly the negative effect of HEBM on the density of the W-7%Ni-3%Fe alloy.

The question of the origins of the increase in the SPS activation energy at long HEBM times (t_{HEBM} = 40 min) is more complex. In our opinion, this effect is caused simultaneously by three factors.

First, it is worth noting that the intensity of the strain-induced dissolving of the tungsten particles can decrease at long HEBM times due to the achievement of the solubility limit of W in the γ-phase. In this case, the increasing of the HEBM time leads to an increase in the creep rate due to an increase in the nonequilibrium degree of the grain boundaries in the γ-phase and a decrease in the grain sizes in the alloy.

The analysis of the XRD phase analysis results shows that the micro-strain of the α-W crystal lattice begins to decrease after 40 min of HEBM (Fig. 5b). This effect can originate from the decrease in the concentrations of the Ni and Fe atoms in the surface layers of the α-W nanoparticles as well as from the decrease in the dislocation density in the α-W particles. The heating of the powders during HEBM is the most probable origin of this effect. The increase in the temperature during HEBM will reduce the distortion degree of the α-W crystal lattice and, as a consequence, the tendency of the nanoparticles to dissolving in the strongly deformed γ-phase. It will lead in an increase in the density of the tungsten alloy.

The increase in the density of agglomerates after 40 min of HEBM is the third probable origin. The increase in the density of agglomerates can originate from the intensive plastic deformation of the tungsten nanoparticles during HEBM as well as from the heating of the samples. The increase in the packing density of the nanoparticles inside the agglomerates will lead to an increase in the initial density of the powder composition W-Ni-Fe and, as a consequence, will provide an opportunity to achieve a higher final density of the tungsten alloy when sintering in the same conditions.

Finally, let us discuss briefly the results of investigations of the mechanical properties of the HTAs. As one can see in Fig. 16a, the dependencies of hardness and yield strength on the grain size

Preprints (www.preprints.org) | NOT PEER-REVIEWED | Posted: 18 April 2023 doi:10.20944/preprints202304.0503.v1

can be described by Hall-Petch relation with a good accuracy. Traditionally, the dependence of the strength characteristics on the grain size in the coarse-grained HTAs is suggested to have more complex character. In particular, the magnitudes of the ultimate strength and of the yield strength in the tension tests depend strongly on the volume fraction of the γ-phase particles as well as on the relations of the lengths of the intergranular boundaries W-W and the ones of the interphase boundaries W-γ [5,11,31,32]. The realization of Hall-Petch effect in the ultrafine-grained HTAs can be a consequence of considerably greater lengths of the grain boundaries that leads to the proportional decrease in the sizes (thicknesses) of the interphase boundaries α-W - γ-phase.

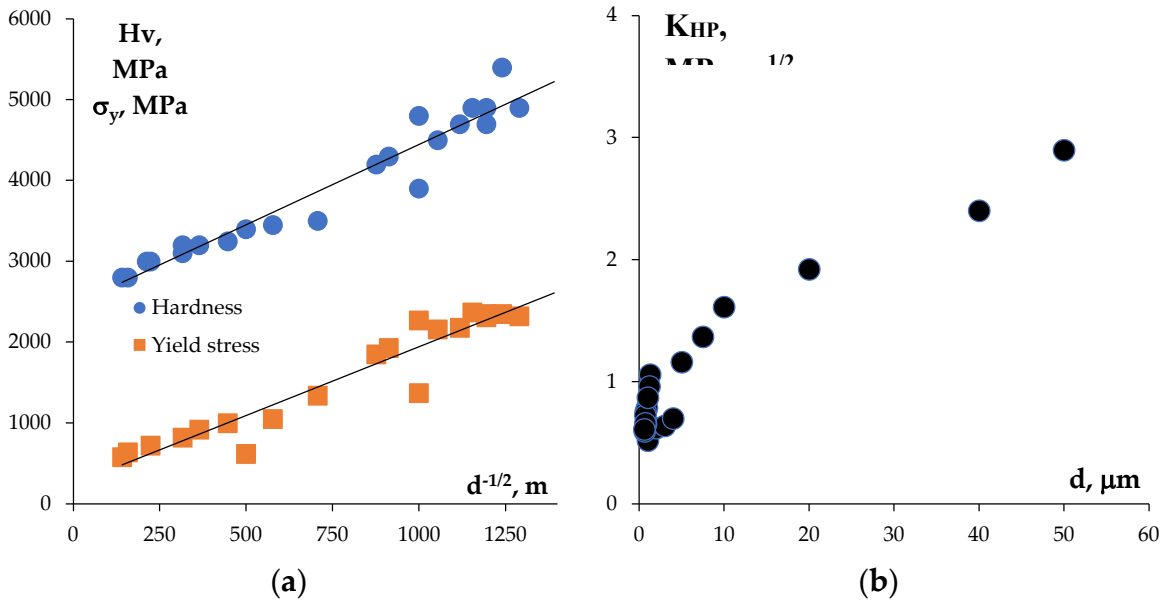

Figure 16. Analysis of investigations of the mechanical properties of the HTAs 90%W-7%Ni-3%Fe: (**a**) dependencies of the hardness and of the yield strength on the grain size; (**b**) dependence of Hall-Petch coefficient on the grain size. Analysis of the results presented in Table 2 and 3.

Knowing the magnitudes of the yield strength σ_y, of the macroelasticity stress σ_0, and of the grain size d one can calculate Hall-Petch coefficient according to the formula $K_{HP} = (\sigma_y - \sigma_0)\cdot d^{1/2}$ for each alloy reflected in Table 2 and 3. Fig. 16b presents the dependence of K_{HP} on the grain size. As one can see in Fig. 16b, the increasing of the sintering temperature and the grain growth lead to an increase in Hall-Petch coefficient. The maximum magnitudes of K_{HP} were achieved in the HTAs sintered at 1450 and 1500 °C (Table 2). In our opinion, this evidences an increase in the adhesion strength of the interphase boundaries with increasing sintering temperature. The increasing of the concentration of the W atoms in the γ-phase can also contribute additionally into the increase in K_{HP}.

No essential differences in the magnitudes of K_{HP} for the alloys obtained from the non-annealed and annealed nanopowders were observed. This allows suggesting the differences in the strength characteristics of the HTAs observed to originate from, first of all, the differences in the grain sizes.

5. Conclusions

1. High Energy Ball Milling (HEBM) of the W-Ni-Fe powders leads to grinding of the tungsten particles and to formation of supersaturated solid solution of W atoms in the γ-phase. After the HEBM, the W nanoparticles have a core – shell structures, which have high concentrations of Ni and Fe atoms in the surface layers of the α-W nanoparticles. This leads to broadening and asymmetry of the α-W XRD peaks.

2. The SPS kinetics for initial fine powders W-7%Ni-3%Fe is governed by the intensity of grain boundary diffusion in the γ-phase. SPS was shown to allow obtaining the samples with increased density, small grain sizes (~1.2-1.3 μm), and increased hardness (4.2-4.3 GPa) as compared to the samples obtained by conventional sintering the fine-grained powders in hydrogen.

Preprints (www.preprints.org) | NOT PEER-REVIEWED | Posted: 18 April 2023 doi:10.20944/preprints202304.0503.v1

3. The SPS kinetics of the nanopowders has two-stage character owing to intensive diffusion Coble creep in the low temperature range and intensive diffusion of W atoms in the crystal lattice of the γ-phase at elevated temperatures. The SPS activation energy in the low heating temperature range is small that originates from the nonequilibrium state of the grain boundaries in the γ-phase with an increased density of defects arising during the HEBM. The recrystallization process in the γ-phase is a possible origin of the change of the diffusion mechanism responsible for the intensity of the nanopowder compaction process in SPS.

4. The relative density of HTAs obtained by SPS was shown to depend on the HEBM time non-monotonously (with a minimum). It was suggested that the effect of reduction of the density is caused by the formation of strongly supersaturated solid solutions of Ni and Fe in the tungsten particles.

5. Annealing the nanopowders in hydrogen was shown to result in a decrease in the sintering activation energy and in an increase in the density of the sintered HTAs. It originates from the decreasing of the oxygen concentration in the nanopowders and an increasing of the Coble diffusion creep rate in SPS.

6. The dependencies of the yield strength and of the hardness on the grain size is described by Hall-Petch equation with a good accuracy. The maximum values of Hall-Petch coefficient were observed for the alloys sintered in hydrogen at elevated temperatures (1450, 1500 °C). This originates from a high adhesion strength of the interphase boundaries as well as probably from the increased concentration of the tungsten atoms in the γ-phase.

Author Contributions: Conceptualization, N.V.M.1 and A.V.N.; methodology, N.V.M.1 and A.V.N.; formal analysis, N.V.M.1, V.N.C. and A.V.N.; investigation, N.V.M.1, N.V.M.2, A.M.B., A.R.F., M.S.B., E.A.L., N.V.S.; resources, V.N.C.; data curation, N.V.M.1 and A.V.N.; writing—original draft preparation, N.V.M.1, V.N.C. and A.V.N.; writing—review and editing, N.V.M.1, V.N.C. and A.V.N..; visualization, N.V.M.1 and A.V.N.; supervision, V.N.C.; project administration, N.V.M.1; funding acquisition, N.V.M.1 All authors have read and agreed to the published version of the manuscript.

Funding: This research was funded by Russian Science Foundation, grant number 22-79-10080.

Data Availability Statement: Not applicable.

Conflicts of Interest: The authors declare no conflict of interest.

Abbreviations: LPS—conventional liquid phase sintering; CG—coarse-grained (alloy); GB—grain boundary; HTA—heavy tungsten alloy; HEBM—high energy ball milling; MA—mechanical activation; OMDs—orientation mismatch dislocations; SEM—scanning electron microscopy; SPS—Spark Plasma Sintering; UFG—ultrafine-grained (alloy); XRD—X-ray diffraction (phase analysis).

Appendix A

Table A1. Microstructure parameters and mechanical properties of HTAs obtained by SPS / FAST

Ref.	Alloy (wt.%)	SPS modes				Characteristics of the HTA			Note [2]
		T_s, °C	V, °C/min	P, MPa	t_s, min	Density (ρ)	d, μm	Mechanical properties [1]	
[22]	W-4Ni-2Co-1Fe	1200-1400	-	30	6	16.78 g/cm^3	0.34	84.3 HRA σ_{ts} = 968 MPa	R_0 = 120 nm t_{HEBM} = 15 h, 226 r/min
[23]	W-5.6Ni-1.4Fe	1230	90	50	0	16.3 g/cm^3 (~92%)	0.72	No data	R_0 = 6 nm t_{HEBM} = 40 h, 226 rpm. Add: Ni_2W_4C, Fe_6W_6C
[24]	W-5.6Ni-1.4Fe	1410	90	30	0	99.4%	~2	No daa	R_0 = 2.44 μm
[25]	W-5.6Ni-1.4Fe	1360	380	30	0	94.8%	6.0	σ_y = 1050 MPa σ_b = 1580 MPa 418 HV_1	R_0 = 2.44 μm
[26]	W-5.6Ni-1.4Fe	1400	105	30	2	~98%	4.4	σ_b = 1700 MPa 418 HV_1	-

Preprints (www.preprints.org) | NOT PEER-REVIEWED | Posted: 18 April 2023 doi:10.20944/preprints202304.0503.v1

		+ cyclic heat treatment 1400 °C				~98%	~6	σ_b = 1780 MPa 489 HV_1	
[27]	W-7Ni-3Fe	1150	100	50	8	96.12%	5-10	σ_b = 1020 MPa 68-69 HRA	R_0 =1-3 μm [3] t_{HEBM} = 5 h, 266 rpm. Add: WC, NiW
[28]	W-5.6Ni-1.4Fe	1320	90	30	0-45	~96%	4-7	No data	R_0 = 2.44 μm
[29]	W-2Mo-7Ni-3Fe	1200	100	50	8	96.42%	4-5	σ_b = 922 MPa 73.8 HRA	R_0 =1-3 μm [3] t_{HEBM} = 40 h, 800 rpm. Add: NiW, Ni_2W_4C, WC
[30]	W-8Ni-2Fe	1000	100	30	0	80.84%	10-20	σ_y = 586 MPa σ_b = 975 MPa 63 HRA	D_{90} =6.3 μm[3] t_{HEBM} = 40 h, 260 rpm
	W-8Ni-2Fe-6Mo					84.61%	5-20	σ_y = 784 MPa σ_b = 1025 MPa 65 HRA	
	W-8Ni-2Fe-12Mo					86.34%	10-20	σ_y = 825 MPa σ_b = 1120 MPa 68 HRA	
	W-8Ni-2Fe-18Mo					93.12%	10-20	σ_y = 950 MPa σ_b = 1160 MPa 72 HRA	
	W-8Ni-2Fe-24Mo					94.25%	15-20	σ_y = 998 MPa σ_b = 1250 MPa 75 HRA	
[31]	W-7Ni-3Fe	1100	100	30	2	68.57%	11.45	σ_y = 475 MPa 138 $HV_{0.5}$	D_{90} =6.2 μm[3] t_{HEBM} = 30 min (in the mortar)
	W-7Ni-3Fe-0.25La_2O_3					87.95%	10.66	σ_y = 497 MPa 357 $HV_{0.5}$	
	W-7Ni-3Fe-0.50La_2O_3					76.83%	9.76	σ_y = 822 MPa 370 $HV_{0.5}$	
	W-7Ni-3Fe-0.755La_2O_3					75.51%	8.88	σ_y = 952 MPa 397 $HV_{0.5}$	
	W-7Ni-3Fe-1La_2O_3					70.44%	7.89	σ_y = 1110 MPa 533 $HV_{0.5}$	
[32]	W-7Ni-3Fe-0.5SiC	1400	100	50	5	93.95%	10-20	σ_y = 1068 MPa 443 $HV_{0.5}$	R_0 = 10 μm [3] t_{HEBM} = 1 h + pressed 600 MPa
	W-7Ni-3Fe-1SiC					90.98%	5-20	σ_y = 810 MPa 458 $HV_{0.5}$	
	W-7Ni-3Fe-1.5SiC					85.05%	5-20	σ_y = 708 MPa 532 $HV_{0.5}$	
	W-7Ni-3Fe-2SiC					82.86%	5-10	σ_y = 729 MPa 564 $HV_{0.5}$	
[33]	W-7Ni-3Fe	1000	100	50	8	~93%	< 1	σ_y = 954.5 MPa 79.3 HRA	R_0 = 2.3-2.7 μm [3] t_{HEBM} = 40 h, 266 rpm
		1250				~87%	3-5	σ_y = 353.6 MPa 63.8 HRA	
[34]	W-2Mo-6Ni-2.5Fe -1.5Co	1000	100	50	8	90.68%	~2	σ_b = 595 MPa 76.14 HRA	R_0 =1-3 μm [3] t_{HEBM} = 20 h, 220 rpm
		1250				98.93%	5.4	σ_b = 1040 MPa 71.43 HRA	
[35]	W-5.6Ni-2.4Fe	1400	100	30	-	~84.8%	12.3	σ_y = 686 MPa σ_t = 975 MPa 385 $HV_{0.5}$	R_0 = 10 μm [3] t_{HEBM} = 1 h Add: Ni-W
	W-5.6Ni-2.4Fe-0.5Co					93.365	11.56	σ_y = 770 MPa σ_t = 961 MPa	

	W-5.6Ni-2.4Fe-1Co					~90.5%	9.48	455 $HV_{0.5}$ σ_y = 1300 MPa σ_t = 1508 MPa 467 $HV_{0.5}$	
	W-5.6Ni-2.4Fe-1.5Co					~87%	9.68	σ_y = 1080 MPa σ_t = 1330 MPa 471 $HV_{0.5}$	
	W-5.6Ni-2.4Fe-2Co					~83%	11.1	σ_y = 1000 MPa σ_t = 1256 MPa 499 $HV_{0.5}$	
[36]	W-21Ni-9Fe	1250	100	40	4	98.6	~10	σ_t = 890 MPa 25.6 HRC	t_{HEBM} = 4 h, 400 rpm
[37]	W-5.6Ni-1.4Fe	1050-1100	100	50	5	98.12	0.871	σ_b = 987 MPa 84.3 HRA	R_0 =100 nm[3] t_{HEBM} = 6 h, 300 rpm
[38]	W-2Mo-7Ni-3Fe	1150	100	50	8	No data	~2	σ_b = 390.1 MPa 69-70 HRA	R_0 =1-3 μm [3] t_{HEBM} = 40 h, 266 rpm Add: Ni_2W_4C

[1] σ_{ts} – transverse rupture strength, σ_b – bending strength, σ_y – yield strength, σ_t – tensile strength.

[2] R_0 is the initial particle size, Add – there are auxiliary phases in the specimens.

[3] the initial particle size of the α-W.

References

1. Green, E.C.; Jones, D.J.; Pitkin, W.R. Developments in high-density alloys. Proc. Symposium of Powder Metallurgy, **1954**, *58*, pp. 253-256.
2. Krock, R.; Shepard, H. Mechanical behavior of the two-phase composite tungsten-nickel-iron. *Transaction of the Metallurgical Society of AIME* **1963**, *227*, 1127-1134.
3. Das, J.; Rao, G.A.; Pabi, S.K. Microstructure and mechanical properties of tungsten heavy alloys. *Materials Science and Engineering A*. 527 (29-30) (2010) 7841-7847. doi:10.1016/j.msea.2010.08.071
4. Povarova, K.B.; Makarov, P.V.; Ratner, A.D.; Zavarzina, E.K.; Volkov, K.V. VNZH-90-type heavy alloys. I. Effect of alloying and the conditions of fabricating tungsten powders on their structure and the properties of sintered alloys. *Russian Metallurgy* **2002**, *4*, 39-48. (in Russian).
5. Sahin, Y. Recent progress in processing of tungsten heavy alloys. *Journal of Powder Technology* **2014**, 764306. doi:10.1155/2014/764306
6. Ishchenko, A.N.; Afanas'eva ,S.A.; Belov, N.N.; Burkin, V.V.; Galsanov, S.V.; Kasimov, V.Z.; Kudryavtsev, V.A.; Lipatnikova, Y.D.; Martsunova, L.S.; Rogaev, K.S.; Sammel', A.Y.; Skosyrskii, A.B.; Yugov, N.T. Destruction features of impactors made of a porous alloy based on tungsten with reinforcing filler when interacting with armored obstacles. *Technical Physics* **2020**, *65*, 414-419. doi:10.1134/S106378422003010X
7. Luo, R.; Huang, D.; Yang, M.; Tang, E.; Wang, M.; He, L. Penetrating performance and "self-sharpening" behavior of fine-grained tungsten heavy alloy rod penetrators. *Materials Science and Engineering A* **2016**, *675*, 262-270. doi:10.1016/j.msea.2016.08.060
8. Ravi Kiran, U.; Panchal, A.; Sankaranarayana, M.; Nandy, T.K. Tensile and impact behavior of swaged tungsten heavy alloys processed by liquid phase sintering. *International Journal of Refractory Metals and Hard Materials* **2013**, *37*, 1-11. doi:10.1016/j.ijrmhm.2012.10.002
9. Ravi Kiran, U.; Sambasiva Rao, A.; Sankaranarayana, M.; Nandy, T.K. Swaging and heat treatment studies on sintered 90W-6Ni-2Fe-2Co tungsten heavy alloy. *International Journal of Refractory Metals and Hard Materials* **2012**, *33*, 113-121. doi:10.1016/j.ijrmhm.2012.03.003
10. Gong, X.; Fan, J.L.; Ding, F.; Song, M.; Huang, B.Y.; Tian, J.M. Microstructure and highly enhanced mechanical properties of fine-grained tungsten heavy alloy after one-pass rapid hot extrusion. *Materials Science and Engineering A* **2011**, *528*, 3646-3652. doi:10.1016/j.msea.2011.01.070
11. Yu, Y.; Zhang, W.; Chen, Y.; Wang, E. Effect of swaging on microstructure and mechanical properties of liquid-phase sintered 93W-4.9(Ni,Co)-2.1Fe alloy. *International Journal of Refractory Metals and Hard Materials* **2014**, *44*, 103-108. doi:10.1016/j.ijrmhm.2014.01.016

12. Das, J.; Kiran, U.R.; Chakraborty, A.; Prasad, N.E. Hardness and tensile properties of tungsten based heavy alloys prepared by liquid phase sintering technique. *International Journal of Refractory Metals and Hard Materials* **2009**, *27*, 577-583. doi:10.1016/j.ijrmhm.2008.08.003
13. Mazilkin, A.A.; Straumal, B.B.; Protasova, S.G.; Bulatov, M.F.; Baretzky, B. Pseudopartial wetting of W/W grain boundaries by the nickel-rich layers. *Materials Letters* **2017**, *192*, 101-103. doi:10.1016/j.matlet.2016.12.049
14. Luo, J.; Gupta, V.K.; Yoon, D.H.; Meyer, H.M. Segregation-induced grain boundary premelting in nickel-doped tungsten. *Applied Physics Letters* **2005**, *87*, 231902. doi:10.1063/1.2138796
15. Fortuna, E.; Sikorsky, K.; Kurzydlowski, K.J. Experimental studies of oxygen and carbon segregation at the interfacial boundaries of a 90W-7Ni-3Fe tungsten heavy alloy. *Materials Characterization* **2004**, *52*, 323-329. doi:10.1016/j.matchar.2004.06.011
16. Krasovskii, P.V.; Samokhin, A.V.; Fadeev, A.A.; Sinayskiy, M.A.; Sigalev, S.K. Alloying effects and composition inhomogeneity of plasma-created multimetallic nanopowders: A case study of the W-Ni-Fe ternary system. *Journal of Alloys and Compounds* **2018**, *250*, 265-275. doi:10.1016/j.jallcom.2018.03.367
17. Parabhu, G.; Kumar, N.A.; Sankaranarayana, M.; Nandy, T.K. Tensile and impact properties of microwave sintered tungsten heavy alloys. *Materials Science and Engineering A* **2014**, *607*, 63-70. doi:10.1016/j.msea.2014.03.130
18. Gryaznov, M.; Samokhin, A.; Chuvil'deev, V.; Fadeev, A.; Alekseev, N.; Shotin, S.; Dorofeev, A.; Zavertyaev, A. Method of W-Ni-Fe composite spherical powder production and the possibility of its application in Selective Laser Melting technology. *Metals* **2022**, *12*, 1715. doi:10.3390/met12101715
19. Chen, H.; Ye, L.; Han, Y.; Chen, C.; Fan, J. Additive manufacturing of W-Fe composites using laser metal deposition: Microstructure, phase transformation, and mechanical properties. *Materials Science and Engineering A* **2021**, *811*, 141036. doi:10.1016/j.msea.2021.141036
20. Chen, H.; Zi, X.; Han, Y.; Dong, J.; Liu, S.; Chen, C. Microstructure and mechanical properties of additive manufactured W-Ni-Fe-Co composite produced by selective laser melting. *International Journal of Refractory Metals and Hard Materials* **2020**, *86*, 105111. doi:10.1016/j.ijrmhm.2019.105111
21. Liu, W.; Ma, Y.; Zhang, J. Properties and microstructural evolution of W-Ni-Fe alloy via microwave sintering. *International Journal of Refractory Metals and Hard Materials* **2012**, *35*, 138-142. doi:10.1016/j.ijrmhm.2012.05.004
22. Krasovskii, P.V.; Samokhin, A.V.; Fadeev, A.A.; Sinayskiy, M.A.; Sigalev, S.K. Alloying effects and composition inhomogeneity of plasma-created multimetallic nanopowders: A case study of the W-Ni-Fe ternary system. *Journal of Alloys and Compounds* **2018**, *750*, 265-275. doi:10.1016/j.jallcom.2018.03.367
23. Tokita, M. Progress of Spark Plasma Sintering (SPS): Method, Systems, Ceramics Applications and Industrialization. *Ceramics* **2021**, 4, 160-198. doi:10.3390/ceramics4020014
24. Mukasyan, A.S.; Rogachev, A.S.; Moskovskikh, D.O.; Yermekova, Zh.S. Reactive spark plasma sintering of exothermic systems: A critical review. *Ceramics International* **2022**, *48*, 2988-2998. doi:10.1016/j.ceramint.2021.10.207
25. Munir, Z.A.; Anselmi-Tamburini, U.; Ohyanagi, M. The effect of electric field and pressure on the synthesis and consolidation materials: A review of the spark plasma sintering method. *Journal of Materials Science* **2006**, *41*, 763-777. doi:10.1007/s10853-006-6555-2
26. Olevsky, E.; Dudina, D. *Field-Assisted Sintering*. Springer Int. Publ., 2018. doi:10.1007/978-3-319-76032-2
27. Chuvildeev, V.N.; Panov, D.V.; Boldin, M.S.; Nokhrin, A.V.; Blagoveshchensky, Yu.V.; Sakharov, N.V.; Shotin, S.V.; Kotkov, D.N. Structure and properties of advanced materials obtained by Spark Plasma Sintering. *Acta Astronautica* **2015**, *109*, 172-176. doi:10.1016/j.actaastro.2014.11.008
28. Li, X.; Xin, H.; Hu, K.; Li, Y. Microstructure and properties of ultra-fine tungsten heavy alloys prepared by mechanical alloying and electric current activated sintering. *Transactions of Nonferrous Metals Society of China* **2010**, *20*, 443-449. doi:10.1016/S1003-6326(09)60160-6
29. Hu, K.; Zheng, D.; Li, Y. SPS densification behavior of W-5.6Ni-1.4Fe heavy alloy powders. *Rare Metals* **2011**, *30*, 581-587. doi:10.1007/s12598-011-0351-z
30. Hu, K.; Li, X.-q.; Yang, Ch.; Li, Y.-y. Densification and microstructure evolution during SPS consolidation process in W-Ni-Fe system. *Transactions of Nonferrous Metals Society of China* **2011**, *21*, 493-501. doi:10.1016/S1003-6326(11)60742-5

31. Li, Y.; Hu, K.; Li, X.; Qu, Sh. Fine-grained 93W-5.6Ni-1.4Fe heavy alloys with enhanced performance prepared by spark plasma sintering. *Materials Science and Engineering A* **2013**, *573*, 245-252. doi:10.1016/j.msea.2013.02.069
32. Li, X.; Hu, K.; Qu, Sh.; Yang, Ch. 93W-5.6Ni-1.4Fe heavy alloys with enhanced performance prepared by cyclic spark plasma sintering. *Materials Science and Engineering A* **2014**, *599*, 233-241. doi:10.1016/j.msea.2014.01.089
33. Xiang, D.P.; Ding, L.; Li, Y.Y.; Chen, G.B.; Zhao, Y.W. Preparation of fine-grained tungsten heavy alloys by spark plasma sintered W-7Ni-3Fe composite powders with different ball milling time. *Journal of Alloys and Compounds* **2013**, *562*, 19-24. doi:10.1016/j.jallcom.2013.02.014
34. Hu ,K.; Li, X.; Qu, S.; Li, Y. Spark-Plasma Sintering of W-5.6Ni-1.4Fe heavy alloys: densification and grain growth. *Metallurgical and Materials Transactions A* **2013**, *44*, 923-933. doi: 10.1007/s11661-012-1454-4
35. Xiang, D.P.; Ding, L.; Li, Y.Y.; Chen, X.Y.; Zhang, T.M. Fabricating fine-grained tungsten heavy alloy by spark plasma sintering of low-energy ball-milled W-2Mo-7Ni-3Fe powders. *Materials Science and Engineering A*. **2013**, *578*, 18-23. doi:10.1016/j.msea.2013.04.065
36. Prasad, B.S.L.; Annamalai, R. A study of molybdenium addition on W-Ni-Fe based heavy alloys sintered with spark plasma sintering. *Bulletin of the Polish Academy of Science. Technical Science* **2019**, *67*, 167-172. doi:10.24425/bpas.2019.128609
37. AyyappaRaj, M.; Yadav, D.; Agrawal, D.K.; Rajan, R.A.A. Microstructure and mechanical properties of spark plasma-sintered La_2O_3 dispersion-strengthened W-Ni-Fe alloy. *Rare Metals* **2020**, doi:10.1007/s12598-020-01390-9
38. Chaurasia, J.K.; Muthuchamy, A.; Patel, P.N.; Annamalai, A.R. Densification of SiC particle reinforced W-Ni-Fe heavy alloy composites through conventional and Spark Plasma Sintering. *Transactions of the Indian Institute of Metals* **2017**, *70*, 2185-2191. doi:10.1007/s12666-017-1041-x
39. Ding, L.; Xiang, D.P.; Li, Y.Y.; Li, C.; Li, J.B. Effects of sintering temperature on fine-grained tungsten heavy alloy produced by high-energy ball milling assisted spark plasma sintering. *International Journal of Refractory Metals and Hard Materials* **2012**, *33*, 65-69. doi:10.1016/j.ijrmhm.2012.02.017
40. Ding, L.; Xiang, D.P.; Pan, Y.L.; Li, Y.Y. Mechanical properties and microstructural evolution of Mo-Co-co-strengthened W-Ni-Fe alloys by spark plasma sintering. *Journal of Alloys and Compounds* **2017**, *712*, 593-598. doi:10.1016/j.jallcom.2017.04.141
41. Senthilnathan, N.; Raja Annamalai, A.; Venkatachalam, G. Microstructure and mechanical properties of spark plasma sintered tungsten heavy alloys. *Materials Science and Engineering A* **2018**, *710*, 66-73. doi:10.1016/j.msea.2017.10.080
42. Wu, Y.; Li, Y.; Yu, D. Fine-grained W-Ni-Fe heavy alloys prepared by Spark Plasma Sintering. *Materials Science Forum* **2016**, *849*, 745-752. doi:10.4028/www.scientific.net/MSF.849.745
43. Jingang, Z.; Weimin, W.; Wei, J.; Qianglong, H.; Aiang, W.; Lin, T.; Kai, Y. Ultrafine grain tungsten heavy alloys with excellent performance prepared by Spark Plasma Sintering. *Journal of Wuhan University of Technology – Mater. Sci. Ed.* **2020**, *35* ,393-398. doi:10.1007/s11595-020-2269-6
44. Ding, L.; Xiang, D.P.; Li, Y.Y.; Zhao, Y.W.; Li, J.B. Phase, microstructure and properties evolution of fine-grained W-Mo-Ni-Fe alloy during spark plasma sintering. *Materials and Design* **2012**, *37*, 8-12. doi:10.1016/j.matdes.2011.12.010
45. Chuvil'deev, V.N.; Nokhrin, A.V.; Boldin, M.S.; Baranov, G.V.; Sakharov, N.V.; Belov, V.Yu.; Lantsev, E.A.; Popov, A.A.; Melekhin, N.V.; Lopatin, Yu.G.; Blagoveshchenskiy, Yu.V.; Isaeva, N.V. Impact of mechanical activation on sintering kinetics and mechanical properties of ultrafine-grained 95W-Ni-Fe tungsten heavy alloys. *Journal of Alloys and Compounds* **2019**, *773*, 666-688. doi:10.1016/j.jallcom.2018.09.176
46. Bragov, A.M.; Chuvil'deev, V.N.; Melekhin, N.V.; Filippov, A.R.; Konstantinov, A.Y.; Sakharov, N.V. Dynamic strength of heavy 90W-7Ni-3Fe alloy produced by Spark Plasma Sintering. *Physical Mesomechanics* **2019**, *22*, 307-312. doi:10.1134/S1029959919040064
47. Dudina, D.V.; Bokhonov, B.B.; Ukhina, A.V.; Anisimov, A.G.; Mali, V.I.; Esikov, M.A.; Batraev, I.S.; Kuznechik, O.O.; Pilinevich, L.P. Reactivity of materials towards carbon of graphite foil during Spark Plasma Sintering: A case study using Ni-W powders. Materials Letters **2016**, *168*, 62-67. doi:10.1016/j.matlet.2016.01.018
48. Bokhonov, B.B.; Ukhina, A.V.; Dudina, D.V.; Anisimov, A.G.; Mali, V.I.; Batraev, I.S. Carbon uptake during Spark Plasma Sintering: Investigation through the analysis of the carbide "footprint" in a Ni-W alloy. RSC Advances **2015**, *98*, 80228-80237. doi:10.1039/C5RA15439A

49. Williamson, G.K.; Hall, W.M. X-ray line broadening from aluminium and wolfram. *Acta Metallurgica* **1953**, *1*, 22-31. doi:10.1016/0001-6160(53)90006-6
50. Kolsky, H. An investigation of the mechanical properties of materials at very high rates of loading. *Proceedings of the Physical Society. Section B* **1949**, *62*,676-700. doi: 10.1088/0370-1301/62/11/302
51. Savenko, V.I.; Toropov, Y.P.; Chernyshev, V.V.; Malkin, A.I. Microstructure and properties of surface-modified tungsten powders mechanically activated in different media. *Physics of Metals and Metallography* **2017**, *118*, 1066-1072. doi:10.1134/S0031918X17110138
52. Duan, B.; Zhou, T.; Yang, G.; Yang, D.; Wang, D. Microstructures and properties of 90W-4Ni-6Mn alloy prepared by vacuum sintering. *Materials Research Express* **2020**, *7*, 036522. doi:10.1088/2053-1591/ab7d5b
53. Farooq, S.; Kemp, P.B.; German, R.M.; Base, A. Effect of initial oxygen content and sintering atmosphere dew point on the properties of tungsten based heavy alloys. *International Journal of Refractory Metals and Hard Materials* **1989**, *8*, 236-243.
54. Frost, H.J.; Ashby, M.F. *Deformation-mechanism maps*. Pergamon Press: London, 1982, 328 p.
55. Young, W.S.; Culter, I.B. Initial sintering with constant rates of heating. *Journal of American Ceramic Society* **1970**, *53*, 659-663. doi:10.1111/j.1151-2916.1970.tb12036.x
56. Coble, R. A model for boundary diffusion controlled creep in polycrystalline materials. *Journal of Applied Physics* **1963**, *34*, 1679-1682. doi:10.1063/1.1702656
57. Lantsev, E.A.; Malekhonova, N.V.; Nokhrin, A.V.; Chuvil'deev, V.N.; Boldin, M.S.; Blagoveshchenskiy, Yu.V.; Andreev, P.V.; Smetanina, K.E.; Isaeva, N.V.; Shotin, S.V. Influence of oxygen on densification kinetics of WC nanopowders during SPS. *Ceramics International* **2021**, *47*, 4294-4309. doi:10.1016/j.ceramint.2020.09.272
58. Lantsev, E.A.; Malekhonova, N.V.; Nokhrin, A.V.; Chuvil'deev, V.N.; Boldin, M.S.; Blagoveshchenskiy, Yu.V.; Andreev, P.V.; Smetanina, K.E.; Isaeva, N.V.; Murashov, A.A. Spark plasma sintering of fine-grained WC hard alloys with ultra-low cobalt content. *Journal of Alloys and Compounds* **2021**, *857*, 157535. doi:10.1016/j.jallcom.2020.157535
59. Lantcev, E.; Nokhrin, A.; Malekhonova, N.; Boldin, M.; Chuvil'deev, V.; Blagoveshchenskiy, Y.; Isaeva, N.; Andreev, P.; Smetanina, K.; Murashov, A. A study of the impact of graphite on the kinetics of SPS in nano- and submicron WC-10%Co powder compositions. *Ceramics* **2021**, *4*, 331-363. doi:10.3390/ceramics4020025
60. Golovkina, L.S.; Orlova, A.I.; Nokhrin, A.V.; Boldin, M.S.; Lantsev, E.A.; Chuvil'deev, V.N.; Sakharov, N.V.; Shotin, S.V.; Zelenov, A.Yu. Spark Plasma Sintering of fine-grained ceramic-metal composites YAG:Nd-(W,Mo) based on garnet-type oxide $Y_{2.5}Nd_{0.5}Al_5O_{12}$ for inert matrix fuel. *Journal of Nuclear Materials* **2018**, *511*, 109-121. doi:10.1016/j.jnucmat.2018.09.006
61. Kolobov, Yu.R.; Grabovetskaya, G.P.; Ivanov, K.V.; Girsova, N.V. Effect of the grain-boundary state and grain size on the mechanisms of creep of submicrocrystalline nickel. *The Physics of Metals and Metallography* **2001**, *91*, 532-537. (in Russian).
62. Chuvil'deev, V.N.; Boldin, M.S.; Dyatlova, Ya.G.; Rumyantsev, V.I.; Ordanyan, S.S. A comparative study of hot pressing and Spark Plasma Sintering of Al_2O_3-ZrO_2-Ti(C,N) powders. *Inorganic Materials* **2015**, *51*, 1047-1053. doi:10.1134/S0020168515090034
63. Chuvil'deev, V.N.; Blagoveshchenskiy, Y.V.; Nokhrin, A.V.; Boldin, M.S.; Sakharov, N.V.; Isaeva, N.V.; Shotin, S.V.; Belkin, O.A.; Popov, A.A.; Smirnova, E.S.; Lantsev, E.A. Spark plasma sintering of tungsten carbide nanopowders obtained through DC arc plasma synthesis. *Journal of Alloys and Compounds* **2017**, *708*, 547-561. doi:10.1016/j.jallcom.2017.03.035
64. Golovkina, L.S.; Orlova, A.I.; Nokhrin, A.V.; Boldin, M.S.; Chuvil'deev, V.N.; Sakharov, N.V.; Belkin, O.A.; Shotin, S.V.; Zelenov, A.Yu. Spark Plasma Sintering of fine-grain ceramic-metal composites based on garnet-structure oxide $Y_{2.5}Nd_{0.5}Al_5O_{12}$ for Inert Matrix Fuel. *Materials Chemistry and Physics* **2018**, *214*, 516-526. doi:10.1016/j.matchemphys.2018.03.091
65. Segal, V.M.; Beyerlein, I.J.; Tome, C.N.; Chuvil'deev, V.N.; Kopylov, V.I. *Fundamentals and Engineering of Severe Plastic Deformation*, New York: Nova Science Publishers, 2010, 542 p.
66. Blaine, D.C.; Park, S.J.; Suri, P.; German, R.M. Application of work-of-sintering concepts in powder metals. *Metallurgical and Materials Transactions A* **2006**, *37*, 2827-2835. doi:10.1007/BF02586115
67. Park, S.J.; Johnson, J.L.; Wu, Y.; Kwon, Y.-S.; Lee, S.; German, M.R. Analysis of the effect of solubility on the densification behavior of tungsten heavy alloys using the master sintering curve approach. *International Journal of Refractory Metals and Hard Materials* **2013**, *37*, 52-59. doi:10.1016/j.ijrmhm.2012.10.016

68. Hu, K.; Li, X.; Qu, S.; Li, Y. Effect of heating rate on densification and grain growth during spark plasma sintering of 93W-5.6Ni-1.4Fe heavy alloys. *Metallurgical and Materials Transactions A* **2013**, *44*, 4323-4336. doi:10.1007/s11661-013-1789-5
69. Larikov, L.N.; Yurchenko, Yu.F. *Diffusion in metals and alloys*; Naukova dumka: Kiev, 1987, 509 p. (in Russian).
70. Park, S.M.; Martin, J.M.; Guo, J.F.; Johnson, J.L. Densification behavior of tungsten heavy alloy based on master sintering curve concept. *Metallurgical and Materials Transactions A* **2006**, *37*, 2837-2848. doi:10.1007/BF02586116
71. Seith, W. *Diffusion in Mettallen*. *Platzwechselreaktionen*, Springer – Verlag, Berlin – Göttigen – Heidelberg, 1955, 381 p.